nanomaterials

MDPI

Review

Theoretical Studies on the Quantum Capacitance of Two-Dimensional Electrode Materials for Supercapacitors

Jianyan Lin, Yuan Yuan, Min Wang, Xinlin Yang and Guangmin Yang *

College of Physics, Changchun Normal University, Changchun 130032, China
* Correspondence: yangguangmin@mail.ccsfu.edu.cn

Abstract: In recent years, supercapacitors have been widely used in the fields of energy, transportation, and industry. Among them, electrical double-layer capacitors (EDLCs) have attracted attention because of their dramatically high power density. With the rapid development of computational methods, theoretical studies on the physical and chemical properties of electrode materials have provided important support for the preparation of EDLCs with higher performance. Besides the widely studied double-layer capacitance (C_D), quantum capacitance (C_Q), which has long been ignored, is another important factor to improve the total capacitance (C_T) of an electrode. In this paper, we survey the recent theoretical progress on the C_Q of two-dimensional (2D) electrode materials in EDLCs and classify the electrode materials mainly into graphene-like 2D main group elements and compounds, transition metal carbides/nitrides (MXenes), and transition metal dichalcogenides (TMDs). In addition, we summarize the influence of different modification routes (including doping, metal-adsorption, vacancy, and surface functionalization) on the C_Q characteristics in the voltage range of $\pm$0.6 V. Finally, we discuss the current difficulties in the theoretical study of supercapacitor electrode materials and provide our outlook on the future development of EDLCs in the field of energy storage.

Keywords: electrical double-layer capacitors; 2D electrode materials; quantum capacitance; first-principle calculations

Citation: Lin, J.; Yuan, Y.; Wang, M.; Yang, X.; Yang, G. Theoretical Studies on the Quantum Capacitance of Two-Dimensional Electrode Materials for Supercapacitors. *Nanomaterials* **2023**, *13*, 1932. https://doi.org/10.3390/nano13131932

Academic Editor: Fabrizio Pirri

Received: 30 May 2023
Revised: 15 June 2023
Accepted: 19 June 2023
Published: 25 June 2023

1. Introduction

In today's world, non-renewable energy sources are decreasing. Energy supply is closely related to environmental issues and basic human needs. Improving the conversion efficiency of energy sources and developing new energy sources has become an urgent problem that needs to be solved in the midst of the energy crisis [1]. In this energy-dependent world, electrochemical devices for energy storage have played a crucial role in overcoming the depletion of fossil fuels [2]. Compared with conventional batteries, supercapacitors have the advantages of high power density, long cycle life, and fast charge and discharge rates. However, the energy density of supercapacitors is usually low, which is a major obstacle to their development [3]. Supercapacitors are usually classified into three types: (1) electrical double-layer capacitors (EDLCs) with ion adsorption through the electrode surface; (2) pseudocapacitors with surface Faraday redox reactions on the electrodes; (3) hybrid supercapacitors that are a mixture of the above two [4,5]. In this paper, we mainly focus on the electrode materials for EDLCs.

For the charging process on EDLCs, the anions and cations in the electrolyte are adsorbed to the positive and negative surfaces, respectively, forming a double-layer due to the external voltage difference. After charging, the anions on the double-layer produce a potential difference between the two plates to store energy. Discharging is the opposite process of charging. Because of the fast rate of this simple physical adsorption process, the EDLCs usually have high power densities. For the electrode materials, carbon materials with a large specific surface area and good electrical conductivity are generally the best choice for the fabrication of EDLCs [4,6–8].

EDLCs have high output power, fast charge and discharge rates, and long service lives but poor energy density [9–11]. Therefore, increasing the energy density of EDLCs has become a key research goal. The energy density of EDLCs is determined by the operating voltage and the specific capacitance of the electrode/electrolyte system [12]. The total interface capacitance (C_T) of EDLCs is related to the quantum capacitance (C_Q) and the double-layer capacitance (C_D), with the expression of $1/C_T = 1/C_Q + 1/C_D$ [13–17]. C_Q, also known as electrode capacitance, reflects the finite quantum state process of the electron-filled system [18,19]. The theoretical prediction of increasing the total EDLC capacitance by increasing the C_Q of the electrode material has been experimentally confirmed [20]. C_Q is proportional to the density of electronic states. A large number of quantum states near the Fermi level can lead to a high C_Q. The electronic structure of a material can be modified by changing the dopants, functional groups, defects, etc. of the structure, thus changing the specific surface area and surface morphology of the electrode material. The larger the specific surface area, the better the energy storage performance of the electrode material [21,22].

Usually, materials with a thickness of a few atomic layers are considered as two-dimensional (2D) materials [3]. Since the discovery of graphene in 2004, 2D materials have experienced rapid development. For example, 2D carbon materials demonstrate excellent properties, such as high specific surface area and high electrical conductivity [23]. Since the working mechanism of EDLCs is an electrostatic effect, the anions and cations on the electrode material surface move to the positive and negative electrodes during the charging and discharging process, forming electric double-layers at the interface. Thus, 2D electrode materials with larger specific surface areas are more suitable for EDLCs than their 3D counterparts [24–27]. However, 2D electrode materials are highly susceptible to stacking due to their high edge activity, resulting in a decreased specific surface area and capacity during reagent application. Numerous studies have been devoted to maintaining or increasing the specific surface area of the electrode materials and improving the circulation rate of anions and cations by changing the morphology of the electrode surface. In this paper, we focus on the aforementioned modification measures (defects, doping changes, adsorption of functional groups, etc.) and atomic exchange on the electrode materials. We summarize the classification of electrode materials and highlight the materials with better performance and greater potential for experimental application.

2. Theoretical Basis

Among many low-dimensional materials, the differential quantum capacitance (C_{diff}) can be defined by

$$C_{diff} = \frac{d\sigma}{d\Phi_{\mathrm{G}}} = \mathrm{e}^2\mathrm{DOS}(-\mathrm{V_e}) \quad (1)$$

in which $d\sigma$ and $d\Phi_G$ represent the differential charge density and differential local potential, respectively.

Thus the magnitude of C_{diff} is dependent on the density of states. The density of states is essentially the number of different states that an electron is allowed to occupy at a given energy level, i.e., the number of electron states per unit volume of energy. Due to quantum confinement effects and the limitation of the low density of states, the significant movement of Fermi levels in two-dimensional materials could accumulate a sufficient number of carriers to provide better energy density, thus improving the performance of supercapacitors.

The excess charge density can be expressed as:

$$\Delta Q = \int_{-\infty}^{+\infty} D(E)[f(E) - f(E - e\phi_G)]dE \quad (2)$$

where $D(E)$ represents the density of states of the system, $f(E)$ is the Fermi-Dirac distribution function, E is the electronic energy with respect to the Fermi level, and e is the fundamental charge. For 2D materials, C_{diff} can be obtained by the following equation:

$$C_{diff} = e^2 \int_{-\infty}^{+\infty} D(E) F_T(E - e\phi_G) dE \quad (3)$$

where $F_T(E)$ is the thermal spreading function, which is obtained from the following:

$$F_T(E) = (4\kappa_B T)^{-1} sech^2\left(\frac{E}{2\kappa_B T}\right) \quad (4)$$

It is also common for researchers to analyze the energy storage capacity of supercapacitors by calculating C_{int}. The C_{int} is obtained by integrating the C_{diff} over the charge and discharge cycles [28,29].

$$C_{int}(V) = \frac{Q}{V} = \frac{1}{V_e} \int_0^V C_{diff}(V') dV' \quad (5)$$

In this paper, C_{diff} is equally defined as C_Q.

3. Research Progress of 2D Electrode Materials for EDLCs

3.1. Graphene-like 2D Main Group Elements and Compounds

Graphene with sp^2 hybridization is a typical representative of 2D materials. [30] In the past decade, graphene-based electrode materials have become a popular research direction for supercapacitor electrode materials. More recently, scientists have tried to discover various analogs with six-membered ring structures that are similar to graphene, such as silicene, germanene, phosphorene, etc. On the other hand, the 2D main group compounds with graphene-like structures, such as 2D carbon nitride (CN), have also been synthesized in recent years. There are also many studies on the performance of 2D CNs as electrode materials.

3.1.1. Graphene

Graphene is prone to stacking due to its high edge activity, resulting in a decrease in specific surface area and capacity. Since graphene oxides are usually used as precursors for graphene preparation, there are many vacancies in graphene-based materials. Many studies have focused on maintaining the dispersion of graphene [31,32].

In 2009, Xia et al. measured the C_Q of monolayer and bilayer graphene, and the curve of C_Q-potential was symmetrical and v-shaped (Figure 1a) [33]. Many scientists have experimentally demonstrated that the capacitance of carbon electrodes can be improved by doping nitrogen (N) atoms or the functionalization of N-containing groups [34–41]. Zhang et al. demonstrated that N-doping changes the electronic structure of graphene and increases the carrier density, which changes the C_Q and leads to an increase in the interfacial capacitance value (Figure 1b) [42]. Yang et al. theoretically investigated the effects of N-doping configuration, N-doping concentration, vacant concentration, and transition metal atoms (Cu, Ag, Au) adsorption on the electronic structure and C_Q of graphene [14]. Their results show that N-doping, vacancy defects, and transition metal atom adsorption can significantly enhance the C_Q of graphene. Among them, the maximum value of C_Q increases from 32.68 to 113.1 μF/cm^2 as the N-doping concentration increases from 1.4% to 12.5% (Figure 1c,d). Mousavi-Khoshdel et al. investigated the changes in C_Q of functionalized graphene with monovalent functional groups (-C_6H_5, -$C_6H_4NH_2$, -$C_6H_4NO_2$, -NH_2) and divalent functional groups (-C_6H_4, -$C_6H_2F_2$, -$C_6H_2Cl_2$, -$C_6H_3CH_3$) [43]. Their results show that the C_Q values of functionalized graphene are higher than that of pristine graphene in both cases. A schematic diagram of the structures of the three types of groups is shown in Figure 1e. Chen et al. investigated the interaction and C_Q of N and S co-doped graphene [44]. The maximum C_Q of pristine graphene is 14 μF/cm^2 and the minimum C_Q is

2.5 μF/cm^2. The C_Q values of pyridine-N-doped graphene and pyrrolic-N-doped graphene at the Fermi level are about 41.4 and 38.2 μF/cm^2, respectively. In a subsequent study, they found that the C_Q value of N/S co-doped graphene could be higher than that of single N-doped graphene, with the highest C_Q value being 95.8 μF/cm^2. However, the C_Q does not improve more when another N or S atom is added to the co-doped system (Figure 1f).

Hirunsit et al. studied the C_Q variation of Al-, B-, N-, and P-doped single-vacancy (V) and multilayer graphene. [28] They showed that Al_1, V, Al_3V, and N_3V modification can increase the C_Q by a large amount (>40 mF/cm^2), and the N_3V structure showed the highest C_Q value, which was 82.18 mF/cm^2 (0.26 V). The construction of multilayer graphene also improves the C_Q (Figure 1g–i). Hu et al. investigated the effect of transition metal (Mn, Fe, Co, Ni) and N atom (TMN_x, x = 1–4) co-doping on the C_Q of graphene [45]. The co-doped systems showed an increase in C_Q, with a maximum value of 180.50 μF/cm^2 for CoN_2 g at −0.3 V (Figure 1j). A similar study was carried out by Wang et al., who explored the C_Q changes of transition metals after in-plane doping and out-of-plane doping on graphene [46]. Their conclusions show that the C_Q of in-plane doping is larger than that of out-of-plane doping, where the charge (Q) of Sc-doped graphene could reach 85 μC/cm^2 at negative bias (Figure 1k). Song et al. studied the variation of C_Q of epoxy (- O -)- and hydroxy (-OH)-modified graphene oxide [47]. The results show that the modified graphene oxide also has a higher C_Q than the original structure. There is a significant increase of C_Q with the increasing oxidation degree on both positive and negative bias (Figure 1l,m).

Sruthi et al. found that the C_Q of graphene can be significantly enhanced by doping on the pristine graphene surface with N, Cl, and P atoms [48]. Additionally, very large C_Q (>600 μF/cm^2) can be achieved when doping N, Cl, and P atoms near room temperature. Xu et al. investigated the C_Q of graphene doped/co-doped with B, N, P, S atoms and vacancy [49]. They also obtained the C_D in a classical 1 M NaCl aqueous solution by using molecular dynamics simulations. Then, the C_T was calculated. Graphene that has been 3N-doped with a single vacancy is supposedly the best candidate as an EDLC electrode (Figure 1n). Zhou et al. investigated the effects of doping (B, N, Al, Si, P, S), vacancies, and Stone–Wales defects on the C_Q of graphene and found that Stone–Wales defects could also improve the C_Q of graphene, but not better than doping or vacancy. The maximum C_Q of Si-VG is 169.76 μF/cm^2 at −0.29 V. The maximum C_Q is 168.90 μF/cm^2 at −0.06 V, when the VG concentration is 5.9% (Figure 1o,p). Zhang et al. determined a variety of materials suitable for supercapacitor applications by systematic calculations and generalizations [50]. They explored the C_Q of 56 species of transition metal atoms and vacancy-doped/co-doped graphene, named TM@G and TM@VG, respectively (Figure 1q). Sruthi et al. explored the effect of different co-doping ratios on the C_Q of graphene [51]. When the dopant ratio C:O:N is 50:8:4, the C_Q of the system at the Fermi energy level can reach 423.73 μF/cm^2 (Figure 1r).

One of the inevitable problems in manufacturing and using graphene materials is the stacking of layers, which significantly affects the structure the electrochemical properties. Cui et al. explored the effect of stacking on multilayered graphene [52]. They assumed a two-layer ab-stacked graphene model, where the top layer is defective and the bottom layer is perfect. They showed that the C_Q of the pristine bilayer graphene increases linearly with voltage, reaching a maximum value of 37.7 μF/cm^2 at 1.0 V. The peak of D2_III has a maximum C_Q of 56.1 μF/cm^2 at a voltage of 1 V (Figure 1s,t). Zhou et al. explored co-doping with N, P, S and transition metals (Ti, V, Cr, Mn, Co, Ni) in monolayer and multilayer graphene [53]. Their study showed that doping with transition metals (TM) improves the C_Q more than co-doping with N, P, and S, and the Ti/Ni and N/P/S co-doped systems exhibit excellent C_Q. However, the C_Q of the multilayer system decreases due to the interactions between the adjacent layers of dopants. In a study by Zeng et al., it was found that the capacitance of B (N)-doped graphene as an anode (cathode) can reach a record C_Q of 4317 F/g (6150 F/g) [54].

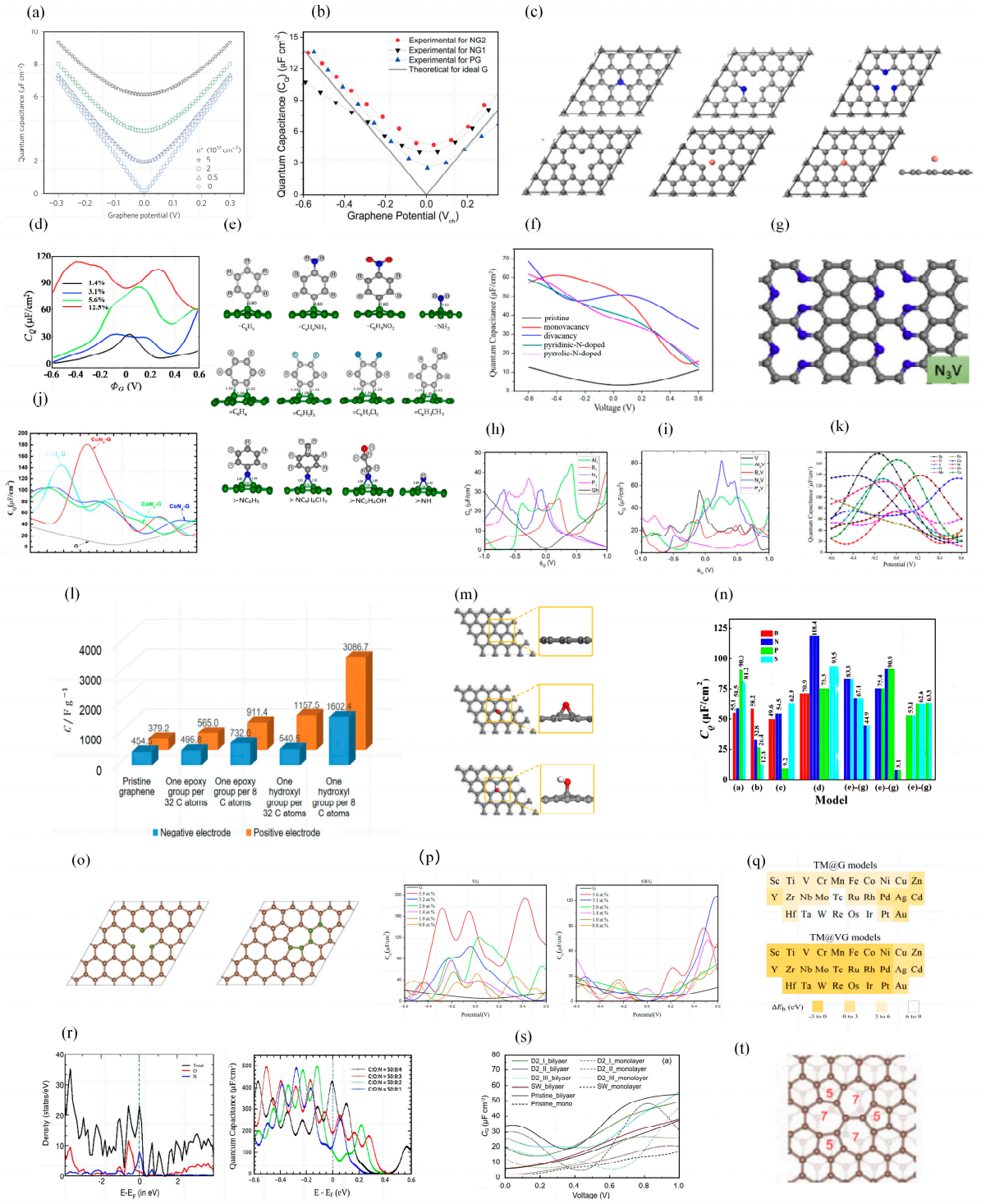

Figure 1. (**a**) C_Q versus potential curves for single- and double-layer graphene. (**b**) Dependence of C_Q on N-dopant concentration as a function of graphene potential (V_{ch}). (**c**) The structures of six defective graphene models. (**d**) C_Q maps of the graphene model with different N-doping concentrations. (**e**) Schematic structures of monovalent, divalent, and trivalent functional groups. (**f**) C_Q-V curves of pristine, cavity, pyridinic-N-doped and pyrrolic-N-doped graphene. (**g**) Structure of 3N-doped and single-vacant graphene (N_3V). (**h**,**i**) C_Q versus potential plot for X_1 and X_3V monolithic graphene structures. (**j**) C_Q versus potential plot for CoN_x (x = 1, 2, 3, 4) co-doped graphene. (**k**) C_Q versus potential plot for graphene doping within the transition metal plane. (**l**) The maximum C_Q in the potential range of −1.5 V~1.5 V for graphene with different oxygen-containing group concentrations

at the negative and positive electrodes. (**m**) Optimized structures of pristine, epoxy graphene and graphene oxide containing hydroxyl groups. (**n**) Change trend chart of the maximum value of C_Q for the B(N, P, S)-doped graphene with different doping models (model-a, model-b, model-c, and model-d) and the N/S, N/P-co-doped the supercell 4 × 4 graphene with different models (model-e, model-f, and model-g). (**o**) Structures of vacancy-defected (VG) and Stone–Wales defected graphenes (SWG). (**p**) C_Q of VG and SWG at different concentrations. (**q**) The stability of TM@G and TM@VG models. (**r**) PDOS and C_Q versus potential curves for N, O co-doped graphene. (**s**) C_Q versus potential for monolayered and bilayered graphene with different defects. (**t**) Configuration of defective bilayer graphene containing D2_11 type (555–777) point defects.

3.1.2. Silicene

Inspired by graphene, silicene is made from 2D layered nanosheets. Silicene sheets with different structures have been successfully synthesized on various substrates. Silicene with a buckling layer structure has a high surface area [55]. It is considered as an excellent anode material for Li-ion batteries because it has enough space to adsorb Li-ions and prevents structural breakage induced by the insertion of Li-ions. Similar to graphene, it is also expected to be one of the ideal electrodes for EDLCs.

Yang et al. explored the effects of vacancy and dopants (N, P, B, and S) concentration on the C_Q of silicene [56]. Their results show that the maximum C_Q of silicene increases with the defect concentration from 1.91 μF/cm^2 at −0.38 V to 102.65 μF/cm^2 at −0.19 V. When the pyridine-N doping concentration is 5.6%, the maximum C_Q is 73.28 μF/cm^2 (−0.07 V). The C_Q is higher than that of the pristine silicene in all modified structures (Figure 2a). Momeni et al. explored the C_Q of pristine silicene, defective silicene, and XSi_3-like silicene (X = Al, B, C, N, P) structures [57]. Their results show that the alternative doped XSi_3-like silicene structures have higher C_Q compared to pristine silicene (C_Q = 1200 F/g) and graphene (C_Q = 500 F/g). The $AlSi_3$ system reaches a maximum C_Q of 2573 F/g under positive bias. They also showed that the large C_Q of XSi_3-like silicene originates from the high electronic states at the Fermi level of 2p and/or 3p orbitals of X and Si atoms, as evidenced by projected density of state analysis (Figure 2b,c). Xu et al. explored the C_Q of silicene with metal atom (Ti, Au, Ag, Cu, and Al atoms) adsorption and single-vacancy doping. [58] It was found that a single vacancy with metal adsorption can significantly increase C_Q. When the Ti concentration is increased from 2% to 12.5%, the maximum value of C_Q increases from 52.2 μF/cm^2 at −0.12 V to 132.2 μF/cm^2 at 0.12 V (Figure 2d).

3.1.3. Germanene

Silicene and Germanene are of great interest as 2D layered nanosheet materials inspired by graphene. Germanene is more prominent than silicene and graphene in terms of its spin–orbit interaction. The large spin–orbit gap (24 meV) of germanene makes it a typical alternative material with the quantum spin Hall effect [59–63]. Moreover, germanene is more easily to be functionalized and has been synthesized by different chemical methods [64–67]. In order to further investigate the electrochemical properties of germanene and probe for more superior performance electrode materials, numerous researchers have investigated the C_Q of germanene with doping, co-doping, and vacancy defects.

Si et al. explored the effect of single vacancy (SV), adsorption of Ti, Au, Ag, Cu, Al atoms, and different doping concentrations on the C_Q of germanene [61]. Similar to graphene and silicene, vacancies can increase the C_Q of germanene, especially in the positive bias range. The C_Q of Ti- and Cu-doped SV germanene is superior to that of Au-, Ag-, and Al-doped ones. Moreover, Ti-doping is more stable in graphene, silicene, and germanene (Figure 2e). Zhou et al. found that transition metal (Ti, Cr, Mn, and Co) doping enhanced the C_Q better than B/N/Al doping [68]. The maximum C_Q can reach 91.47 μF/cm^2 (0.2 V) for Ti-doping near the Fermi level. The co-doped system improves C_Q more than single-doping (Figure 2f). Si et al. further investigated the effects of doping/co-doping, vacant defects, and multilayer structure on the electronic structure and C_Q of

germanene [69]. Their results show that N-doping can significantly improve the C_Q of germanene. In a study of single and multilayered germanene co-doped with NAl, NNAl, NPAl, and NSAl, it was found that the interlayered interactions contributed more to the increase in C_Q (Figure 2g).

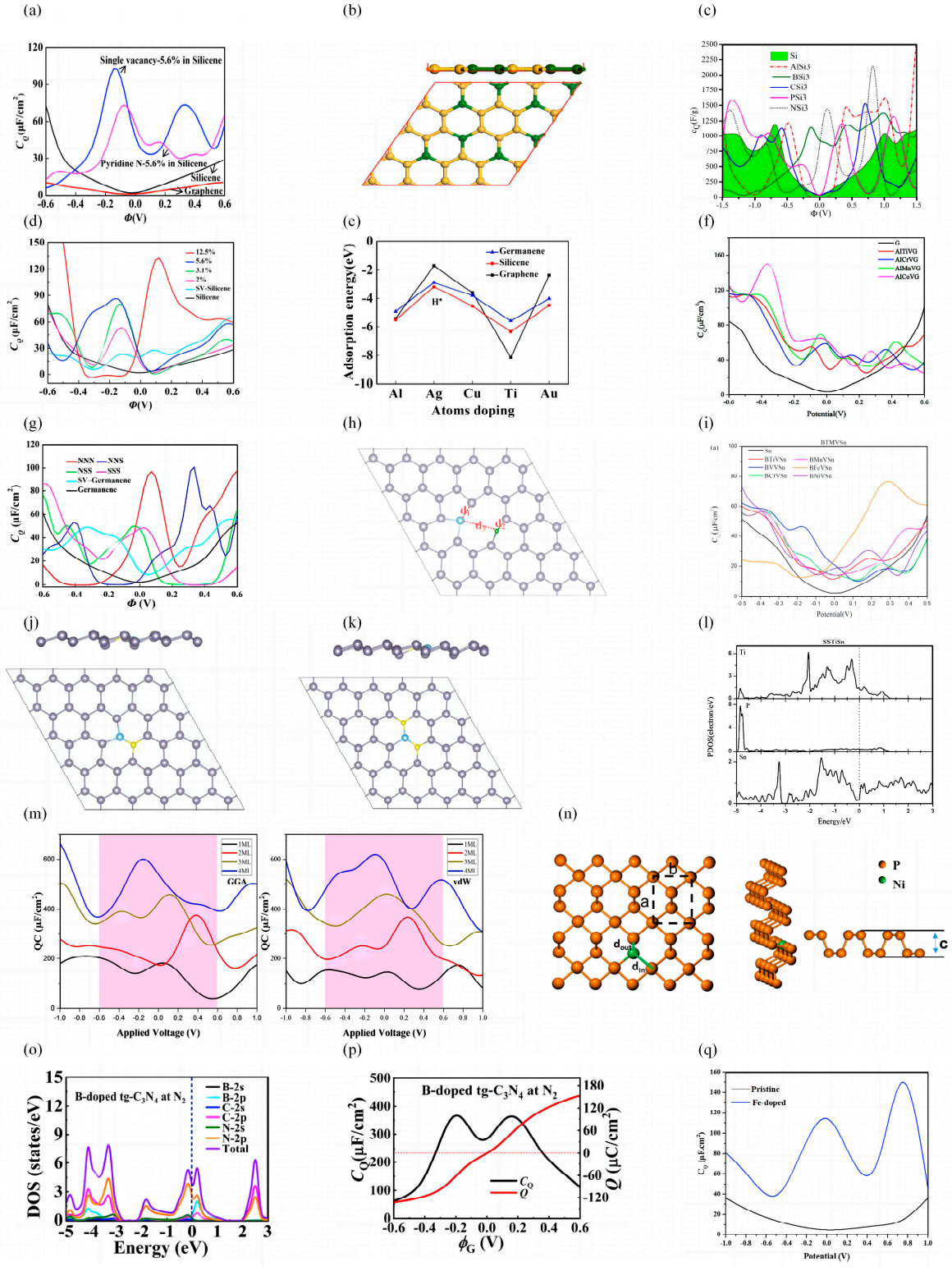

Figure 2. (**a**) C_Q versus potential plot for single vacant and pyridine-N-doped silicene. (**b**) Schematic diagram of the atomic structure of 2D $AlSi_3$. (**c**) C_Q versus potential curves for pristine and X-doped

silicene (X = Al, B, C, P, N). (**d**) C_Q versus potential plot for single vacant silicene adsorbed with different Ti concentrations. (**e**) Adsorption energy of metal atoms on defective germanene, silicene, and graphene. (**f**) The plot of C_Q versus potential for defective germanene co-doped with Ti, Cr, Mn, Co, and Al. (**g**) C_Q versus potential curves for N/S co-doped single vacant germanene. (**h**) Structure of B and transition metal atoms co-doped with defective stanene. (**i**) C_Q versus potential plot for BTMVSn. (**j**,**k**) Structures of S and Ti atoms co-doped and line-doped stanene. (**l**) TDOS diagram of SSTiSn. (**m**) C_Q diagrams of multilayered boronene. (**n**) Structure of Ni-doped phosphorene. (**o**,**p**) DOS and C_Q diagrams of B-doped *tg*-C_3N_4. (**q**) C_Q versus potential plots for iron-doped BC_3 monolayer.

3.1.4. Stanene

Stanene is a novel material that has received increasing attention in recent years. It has been successfully realized by epitaxial growth on Bi_2Te_3 (111) substrates [70–72]. Stanene exhibits several remarkable features, including large spin–orbit gaps, topological superconductivity, quantum anomalous Hall behavior, giant magnetoresistance, and efficient thermoelectricity [73]. Additionally, there have been numerous studies showing that measures such as doping with metal atoms can have a large effect on the structural and electrochemical properties of Stanene [74,75].

Zhou et al. verified the effect of vacancies and the single-doping and co-doping of light element atoms (B, N, Al, Si, P, S) and transition metals (Ti, V, Cr, Mn, Fe, Ni) on the geometry, electronic structure, and C_Q of stanine [76]. Their results show that vacancy, doping, and co-doping can improve the C_Q of stanene and that co-doped defective stanene exhibits better C_Q at negative potentials than at positive bias, indicating that it can be used as a good anode material. The maximum C_Q of BFeVSn is 76.52 μF/cm^2 (0.29 V) under positive bias conditions (Figure 2h,i). Zhou et al. also investigated the effect of N/P/S and line co-doping with heavy metals (Ti, V, Fe, Ni) on stanine [77]. The effect of line co-doping to improve the C_Q of the system is more obvious, where the maximum C_Q at a positive bias of SSTiSn is 77.18 μF/cm^2, which could be attributed to the increased electronic states of the Ti dopant and adjacent Sn atoms (Figure 2j–l).

3.1.5. Boronene

Due to the high carrier concentration, boronene has been used in plasma devices, extending the functionality to the visible region. Boronene is predicted to be an excellent candidate for Li-ion batteries due to its high Li capacity [78–80].

Kolavada et al. theoretically analyzed the C_Q of δ-6 boronene with different layer numbers in aqueous electrolytes (AEs) and ionic liquid electrolytes (ILEs) [81]. In both AE and ILE systems, C_Q enhances as the number of layers increases from 1 monolayer (ML) to 4 ML. When the number of layers is 4 ML, C_Q can reach more than 600 μF/cm^2 in both systems (Figure 2m).

3.1.6. Phosphorene

Phosphorene is a relatively new member to the group of 2D materials discussed in this study. Its strong in-plane anisotropy makes phosphorene a unique material for novel electronic devices [82–86]. Zu et al. fabricated supercapacitors by using phosphorene as electrodes and with the discharge capacity of 3181.5 F/g in a three-electrode configuration [87].

Ramesh et al. computationally examined the effect on phosphorene when half-metal (Si)-dopants, active-nonmetal (S)-dopants, and two transition metal (Ti, Ni) dopants replace the P atom [88]. The C_Q of pristine phosphorene is approximately symmetric, with a minimum value of 2.27 μF/cm^2 at the Fermi level. The C_Q of all substitution systems is higher than that of the pristine phosphorene, with the highest C_Q value of 92.1 μF/cm^2 for Ti-doping at 0.4 V (Figure 2n).

3.1.7. Main Group Compounds

In recent years, four 2D carbon nitride (CN) structures, *hg*-C_3N_4, *tg*-C_3N_4, C_2N, and C_3N have been experimentally synthesized to further enrich the 2D electrode materials for supercapacitors [89–91]. These CN structures have high specific surface areas and excellent electrochemical stability. Therefore, CNs are considered good electrode materials.

Chen et al. investigated the effects of B and O doping on the electronic properties and C_Q of 2D CNs. They found that doping with B or O could convert CNs from semiconductors to metals, thus improving the electrical conductivity [92]. The C_Q values of B-doped CNs are all higher than those of B-doped monolayer graphene. The increased C_Q can mainly be attributed to the strong hybridization between the dopant and the adjacent C and N atoms (Figure 2o,p).

Majdi et al. investigated the electrochemical properties of a new 2D Fe-doped boron carbide monolayer (FBC_3ML) [93]. The maximum C_Q of FBC_3ML increases to 150.09 μF/cm^2 compared to the original BC_3ML, and the C_Q-V curve becomes symmetric (Figure 2q).

3.2. Transition Metal Carbides or Nitrides (MXenes)

MXenes are 2D-layered materials derived from transition metal carbides, nitrides, or carbonitrides [94]. MXenes can be produced by selectively removing the A-layer from MAX phases, the 3D precursors of MXenes, noted as $M_{n+1}AX_n$ phases (n = 1, 2 and 3). MAX phases are generally divided into three types: 211, 312, and 413 structures. M denotes early transition metal elements (such as Sc, Ti, Zr, Hf, V, Nb, Ta, Cr, Mo, etc.); A denotes elements of group 13 or 14, such as Al or Si; and X refers to C, N, or their mixtures [2]. MXenes are often used in the field of energy storage because of their special physical and chemical properties.

The first MXene, Ti_3C_2, was isolated from Ti_3AlC_2 powder by immersing it in a hydrofluoric acid solution [94]. Subsequently, many MXene family members have been synthesized using selective etching methods and many new MXene structures have been theoretically predicted [2]. When performing chemical etching methods, the metal atoms on the MXene's surface can easily react with -H, -O, -F, and -OH groups in solution and terminate them on the MXene's surface, thus giving rise to functionalized MXenes, $M_{n+1}X_nT_x$, where T is the surface termination group [95–97]. This surface functionalization usually has an impact on the energy storage capacity of MXenes. Since the MAX phases usually have carbon vacancies (V_C) [98,99], MXenes derived from the MAX phases are considered to have the same nature of carbon vacancies. The treatment of MXene materials via doping and vacancy also cause changes in the C_Q of the materials. The current research on the C_Q of MXene materials after modulation is more comprehensive. In this section, the effect of various modulation means on the C_Q performance of MXene electrode materials will be discussed separately according to the different M elements.

3.2.1. $Ti_{n+1}C_nT_x$

As the first successfully prepared MXene, Ti_3C_2 and its isomer Ti_2C have received increasing attention as electrode materials for supercapacitors [100,101].

Si et al. focused on the modulation of the two Ti-C MXenes materials using doping, vacancy, and adsorption methods [102]. Their calculations show the pristine structures have higher C_Q compared to the functionalized Ti_3C_2 and Ti_2C. The C_Q of the functionalized structures decrease in an order of OH > F > H > O. The maximum C_Q of OH groups adsorbed on Ti_3C_2 and Ti_2C near the Fermi level is 264.414 μF/cm^2 (0 V) and 276.960 μF/cm^2 (−0.12 V) (Figure 3a,b). On the other hand, the adsorption of metal atoms on the surface of Ti_3C_2 and Ti_2C can also change their C_Q considerably. It is shown that on Ti_3C_2, the adsorption of Al atoms significantly increases the C_Q (398.193 μF/cm^2 at −0.072 V) due to the increase of the low potential local electronic states. A similar trend also appears for Ti_2C, where Ti_2C-Al has a maximum C_Q of 444.192 μF/cm^2 (0.312 V) near the Fermi level (Figure 3c,d). Furthermore, they have found that the adsorption of Ca atoms on $Ti_3C_2F_2$ significantly improves the energy storage performance of the system with a C_Q

value of 488.153 μF/cm^2. Nevertheless, the C_Q of the Ti_2C system shows no clear change (Figure 3e,f) [102].

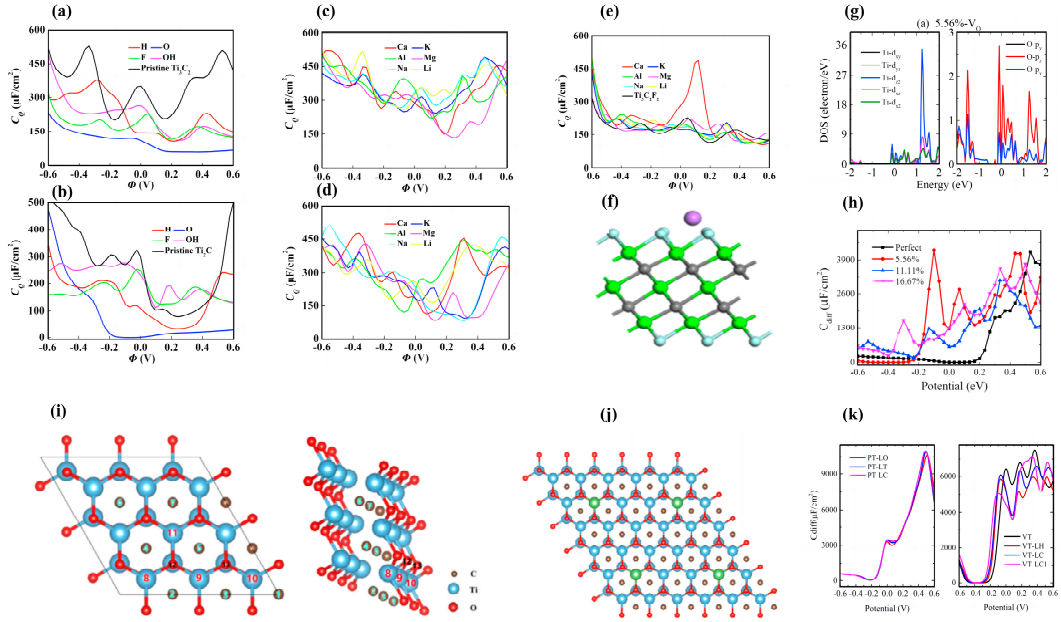

Figure 3. (**a**,**b**) C_Q diagrams of functionalized Ti_3C_2 and Ti_2C. (**c**,**d**) C_Q diagrams of metal atoms-adsorbed Ti_3C_2 and Ti_2C. (**e**) C_Q diagram of metal atoms-adsorbed $Ti_3C_2F_2$. (**f**) Structure of $Ti_3C_2F_2$ adsorbed by metal atoms. (**g**) PDOS diagram of Ti_2CO_2 with an oxygen vacancy concentration of 5.56%. (**h**) C_Q diagram of Ti_2CO_2 with different oxygen vacancy concentrations. (**i**) Schematic diagram of the vacant defected Ti_2CO_2 structure by removing atoms with atomic numbers (2), (3, 4), (1, 5, 6) and (3, 5, 7), denoted as CVL1, CVL2, CVL3, and CVL4, respectively. (**j**) The optimized structures of PT-LT monolayer. The red, light blue, brown, and light green balls denote the oxygen, titanium, carbon, and lithium atoms, respectively. (**k**) C_Q diagrams of Li atoms adsorbed on Ti_2CO_2 (PT) and C-vacant Ti_2CO_2 (VT) monolayers.

Bafekry et al. investigated the oxygen vacancies in the Ti_2CO_2 monolayer and confirmed its semi-metallic properties by calculating the density of states of the system [103]. To further investigate the effect of O vacancy concentration on the properties of Ti_2CO_2, Su et al. systematically explored the C_Q of Ti_2CO_2 with different O vacancy concentrations [104]. Their results demonstrate that the O vacancy concentration has a strong effect on C_Q. The pristine Ti_2CO_2 has a low C_Q under negative bias, with a maximum value of 4204.4 μF/cm^2 (0.53 V). When one oxygen vacancy (5.56%) is introduced, the maximum C_Q values increase to 4263.85 μF/cm^2 (−0.1 V) and 4142.0 μF/cm^2 (0.43 V) for negative and positive potentials, respectively. However, the maximum C_Q decreases when two or three oxygen vacancies are introduced. The DOS of Ti_2CO_2 near the Fermi level mainly originates from O-p_z and Ti-d orbitals. They speculate that the introduction of oxygen vacancies increases the charge transfer between adjacent O and Ti atoms (Figure 3g,h) [104]. While Li et al. theoretically investigated the C_Q of Ti_2CO_2 monolayer with carbon vacancy line (CVL) [105]. The introduction of CVL improved the C_Q and Q of the system under negative and positive bias within ±0.6 V. The CVL4 system improves the maximum C_Q of 469.7 μF/cm^2 under negative bias compared to the pristine Ti_2CO_2 monolayer (Figure 3i). Li et al. calculated the C_Q of pristine Ti_2CO_2 (PT) and C-vacant Ti_2CO_2 (VT) monolayers adsorbed by Li atoms. [106] From their results, it can be seen that the maximum C_Q of PT-LT monolayer is 10,993 μF/cm^2 (0.48 V), the maximum C_Q of VT monolayer is 7592 μF/cm^2 (0.36 V), and the maximum C_Q of VT-LC1 is 6866 μF/cm^2 (0.54 V), within the positive bias voltage (Figure 3j,k).

3.2.2. $Sc_{n+1}C_nT_x$

Sc-based MXenes have the lightest M atom. Among them, Sc_2CF_2 is a semiconductor with strong anisotropic carrier mobility and thermal conductivity. The electron mobility of Sc_2CF_2 in the zigzag direction is almost four times higher than that of phosphorene in the armchair direction, and its thermal conductivity is higher than that of most low-dimensional metals and semiconductor materials. Due to its excellent properties in electronic devices, Sc_2CF_2 has received much attention in recent years [107,108].

Cui et al. studied the exchange defects of Sc/F, Sc/C, and C/F atoms (Figure 4a) [109]. Their study shows that the atomic exchange has little effect on the semiconducting properties. Additionally, the maximum C_Q of pristine Sc_2CF_2 under negative bias is 739.39 μF/cm^2 (−0.48 V). The atomic exchange of C/F atoms and C/Sc atoms reduces the maximum C_Q of Sc_2CF_2 monolayer under negative bias to 488.60 μF/cm^2 (−0.44 V) and 282.57 μF/cm^2 (−0.48 V), respectively. The atomic exchange between F and Sc atoms increases the maximum C_Q of Sc_2CF_2 monolayer under negative bias to 1037.76 μF/cm^2 (−0.48 V). Cui et al. also studied the C_Q of Sc_2CT_2 (T = F, P, Cl, Se, Br, O, Si, S, OH) monolayers (Figure 4b) [110]. They found that the maximum C_Q of the Sc_2C monolayer in aqueous electrolyte (±0.6 V) is 1025.01 μF/cm^2 and 1297.03 μF/cm^2 under negative and positive bias, respectively. Compared with the original Sc_2C structure, the maximum C_Q under the negative bias of Sc_2CT_2 (T=P, Cl, Se, Si) increases, with the maximum C_Q of Sc_2CP_2 being 3800.34 μF/cm^2. The maximum C_Q of the Sc_2CSi_2 monolayer increases to 1708.82 μF/cm^2 under positive bias voltage, but the maximum C_Q of all other systems decreases under the positive bias voltage. However, all of them have a larger maximum C_Q than the system with Sc_2CF_2 for atomic exchange.

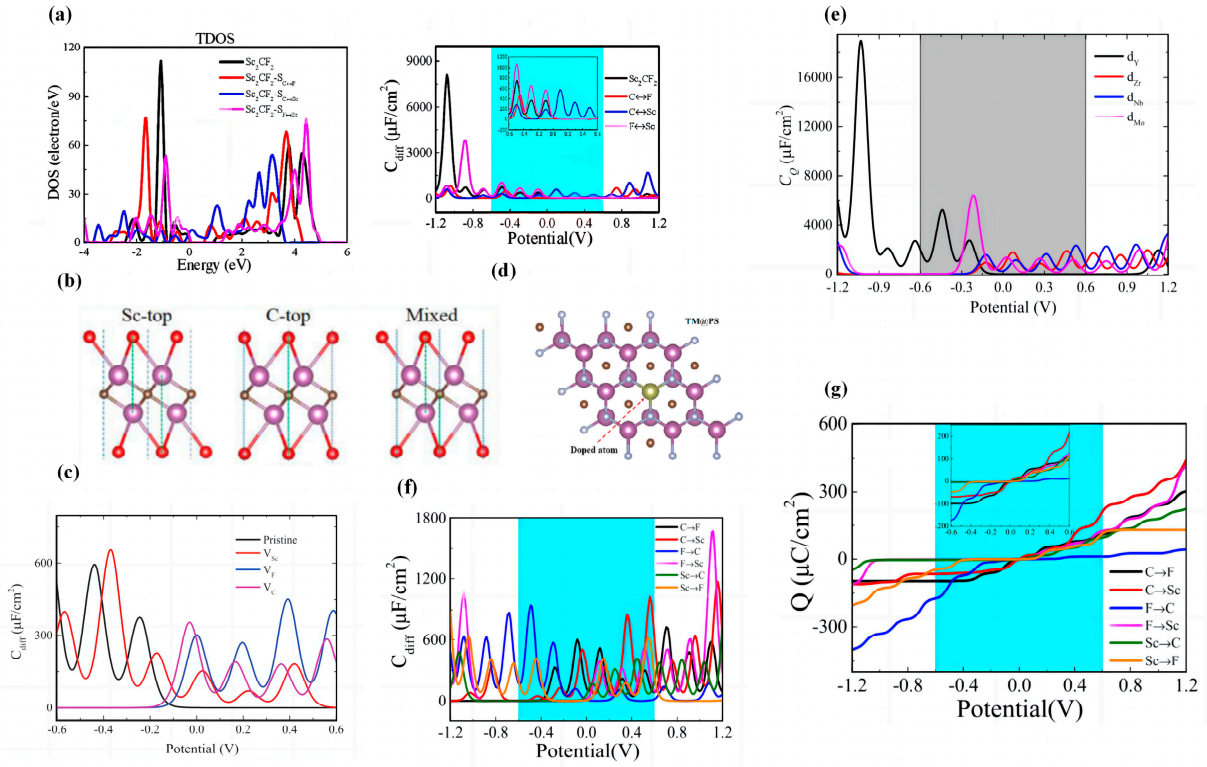

Figure 4. (**a**) TDOS and C_Q of Sc_2CF_2-SC↔F, Sc_2CF_2-SC↔Sc, and Sc_2CF_2-SF↔Sc atomic exchange monolayers. (**b**) Three possible configurations of Sc_2CT_2, namely Sc-top, C-top, and hybrid configurations. (**c**) C_Q of three vacancy-defective systems formed by removing a C, F, or Sc atom from Sc_2CF_2. (**d**) Schematic diagram of Sc_2CF_2 replacing one Sc atom for doping. (**e**) C_Q versus potential plot for Sc_2CF_2 doped with 4d TM atoms (including Y, Zr, Nb, and Mo). (**f**) The plot of C_Q versus potential for atomic exchanged Sc_2CF_2. (**g**) Charge versus potential for atomic exchanged Sc_2CF_2.

Subsequently, Cui et al. theoretically studied the C_Q of Sc_2CF_2 with different atomic vacancies (Figure 4c) [111]. They observe that, at positive bias, pristine Sc_2CF_2 has almost no C_Q, while the introduction of vacancies increases it. The maximum C_Q of Sc_2CF_2-VF at positive bias is 493 μF/cm^2 (0.40 V). It is noteworthy that the C_Q of all systems with vacancies at the Fermi level is larger than that of the original system. Rui et al. investigated the C_Q of doped Sc_2CF_2 with 13 transition metal atoms (Figure 4d) [112]. Fe-doped Sc_2CF_2 shows a symmetry C_Q-V curve, with a maximum C_Q of 5407.6 μF/cm^2 at 0 V. All the 4d transition metal atoms-doped Sc_2CF_2 structures show asymmetric C_Q-V curves. The maximum C_Q of the Mo-doped system at negative bias is 6917.88 μF/cm^2 at −0.2 V. For the Nb-doped system, the maximum C_Q is 2599.72 μF/cm^2 at 0.52 V under positive bias (Figure 4e). For 5d transition metal dopants, the maximum C_Q is 1833.15 μF/cm^2 (0.48 V) in the Re-doped system. Cui et al. also studied the geometry, electronic properties, and C_Q of Sc_2CF_2 with intrinsic defects [113]. They found that the C_Q fluctuations are more pronounced for systems with defects. Among them, the maximum C_Q of Sc_2CF_2-dF→C and Sc_2CF_2-dC→Sc monolayers are 924.69 μF/cm^2 (−0.48 V) and 1024.03 μF/cm^2 (0.56 V), respectively (Figure 4f). In their study, the charge (Q) of the Sc_2CF_2-dF→C monolayer was mainly stored in the negative potential (Figure 4g).

3.2.3. $Hf_{n+1}C_nT_x$

Most functionalized MXenes have metallic properties, while Hf_2CO_2 has a moderate band gap and good thermal conductivity [114,115].

Liu et al. studied the C_Q of Hf_2CT_2 (T = -O, -F, -S, -Cl, -OH, -Se) [116]. Their results show that the maximum C_Q value of Hf_2C is 549 μF/cm^2 (0.56 V). At positive bias, the C_Q of the other functionalized systems (T = -O, -S, -Se) are smaller than the original system. The C_Q of Hf_2CO_2 is almost zero at positive bias. The maximum C_Q of Hf_2CSe_2 at negative bias is 564 μF/cm^2 (−0.56 V). The maximum C_Q of $Hf_2C(OH)_2$ is 804 μF/cm^2 at 0.44 V (Figure 5a). In experiments, mixed terminations are often randomly attached to the surface of MXenes during etching; thus, there are various configurations of surface coverage and mixed terminations. The surfaces of MXenes are often bound by mixed terminations, mainly -O, -F, and -OH [117]. Therefore, Liu et al. considered MXene groups with a mixed termination of -O, -F, and -OH [116]. The results show the symmetrical characteristics of C_Q-V curves for all three groups, with the highest C_Q at zero potential of 778.82, 552.17, and 177.97 μF/cm^2, respectively (Figure 5b).

Liu et al. also computationally investigated the effect of N doping concentration on the electronic properties and C_Q of Hf_2CO_2 [118]. Based on the calculation results, the C_Q of Hf_2CO_2 systems with doping concentrations of 11%, 22%, 33%, and 44% are relatively low at negative bias. The maximum C_Q of the pristine Hf_2CO_2 system (PH) is 84.06 μF/cm^2. The maximum C_Q values of PH-33% and PH-100% at positive bias are 423.62 μF/cm^2 and 441.16 μF/cm^2, respectively. The maximum C_Q of PH-78% is 1208 μF/cm^2. Thus, it indicates that the N-doping concentration also changes the C_Q of Hf_2CO_2 monolayer. (Figure 5c) Subsequently, Liu et al. further investigated the maximum C_Q of PH and the doped systems at different temperatures [118]. They noted that the maximum C_Q decreased with increasing temperature for all systems except PH-22%. Among all systems, the maximum C_Q is 1535.2 μF/cm^2 at 233 K for the PH-78% system (Figure 5d). As with their previous studies, they also considered the case of mixed terminals. Their results show that the maximum C_Q is increased for all other systems after N-doping. As the doping concentration increases, the C_Q-V curve becomes more symmetrical (in the range of ±0.6 V).

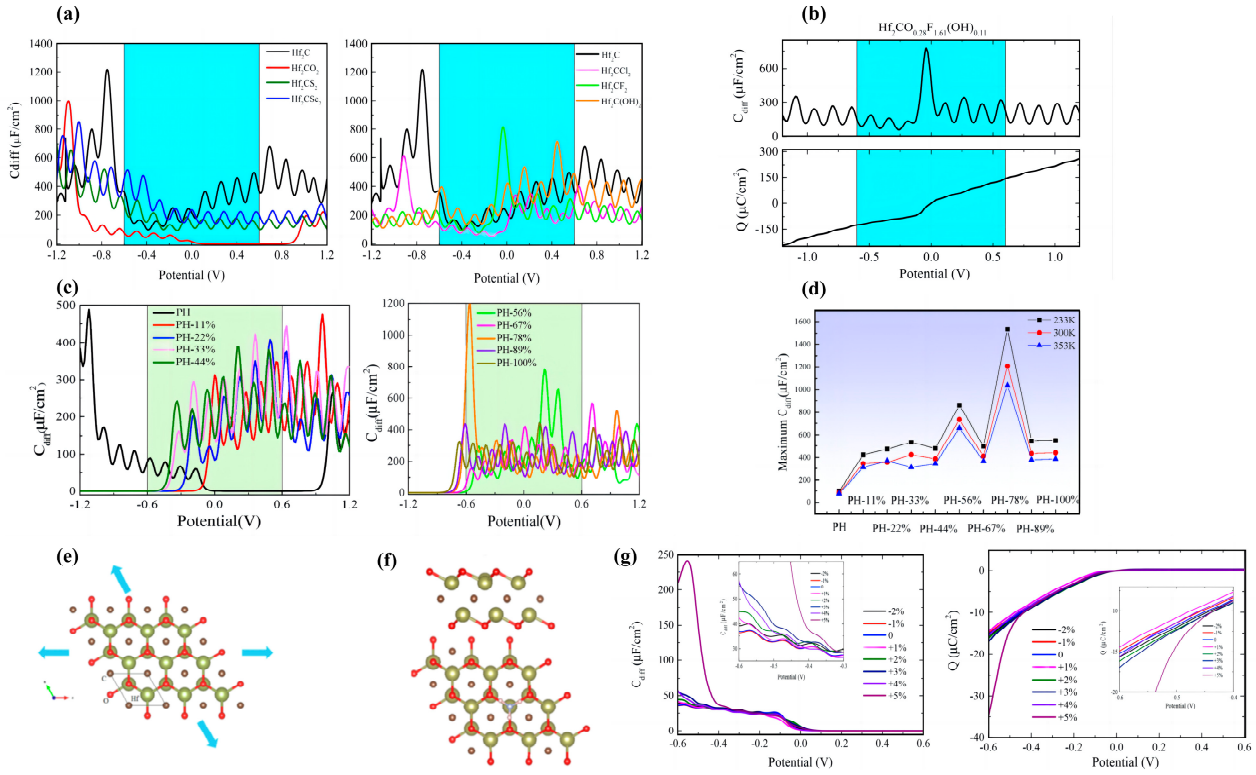

Figure 5. (**a**) The plot of C_Q versus potential for Hf_2CT_2 (T = -O, -F, -S, -Cl, -OH, -Se). (**b**) The plots of C_Q and surface charge versus potential for the mixed terminal of -O, -F, and -OH groups in Hf_2C. (**c**) C_Q versus potential plot of Hf_2CO_2 with different N-doping concentrations. (**d**) The maximum C_Q of Hf_2CO_2 with different N-doping concentrations at 233 K, 300 K, and 353 K (**e**) Top and side views of the Hf_2CO_2 monolayer, where the applied biaxial strain is along the *a* and *b* directions. (**f**) Schematic diagram of the site of the NH_3 molecule adsorption. (**g**) C_Q and surface charge versus potential plots for NH_3-adsorbed Hf_2CO_2 under different strain magnitudes.

More interestingly, Cui et al. explored the C_Q of Hf_2CO_2 monolayers under bi-axial strain [119]. Strain is a common strategy to modulate the properties of materials, which can tune the electronic structure of the material, thus affecting many physical properties of the material. For example, it has been experimentally demonstrated that the introduction of tensile strain can lead to a transition from direct to indirect bandgap in the MoS monolayer, which expands the light absorption range and reduces the complexation of photogenerated carriers. Cui et al. have demonstrated that strain can significantly modulate the electronic structure of Hf_2CO_2 monolayers, which has a very important impact on the material properties [119]. The results show that the maximum C_Q values of strain-free Hf_2CO_2 are 1.57 μF/cm^2 (0 V) and 78.99 μF/cm^2 (−0.6 V) under positive and negative bias, respectively. Under positive bias, the maximum C_Q of the Hf_2CO_2 monolayer increases at all strains except 3%. Under negative bias, the maximum C_Q of the Hf_2CO_2 monolayer increases at all strains except −6%, −4%, and −2% (Figure 5e). Li et al. explored the effect of adsorption of NH_3 on pristine Hf_2CO_2 and varying its biaxial stress [120]. In the range of ±0.6 V, the C_Q-V curve of Hf_2CO_2 under strain is asymmetric. The C_Q at negative potentials is significantly higher than that at positive potentials, and the maximum C_Q of Hf_2CO_2 under free strain is 38.75 μF/cm^2 at −0.57 V. The maximum C_Q increases gradually with increasing tensile strain and reaches a maximum of 244.27 μF/cm^2 at +5% strain (Figure 5f,g).

3.2.4. $Zr_{n+1}C_nT_x$

Zr_2CO_2 is an excellent functionalized MXene with many excellent properties. Due to its excellent photovoltaic properties and high hole mobility, it can be considered as a suitable photocatalyst [121,122].

Xu et al. investigated the electronic properties and C_Q of pristine, doped, and single C vacant (VC) Zr_2CO_2 [123]. The doped atoms were chosen as Y = Si, Ge, Sn, N, B, S, F (Figure 6a,b). The doped atoms had a significant effect on C_Q and Q. The maximum C_Q of pristine Zr_2CO_2 was 407 μF/cm^2 (−0.6 V) and 32.3 μF/cm^2 at the Fermi level. The introduction of C vacancies increased the C_Q at positive bias. The introduction of all the considered dopant atoms increased the maximum C_Q, and B doping at negative bias increased the maximum C_Q to 1993 μF/cm^2. The maximum C_Q of S-doped structure was 3293.7 μF/cm^2 (0.4 V). At 0 V, a significant increase in C_Q can be observed in the systems doped with VC, F, N and S atoms. Xu et al. also explored the maximum C_Q of pristine Zr_2CO_2, Zr_2CO_2-VC, and doped Zr_2CO_2 at different temperatures [123]. Similar to the trend of C_Q with temperature for N-doped Hf_2CO_2, they noted that the maximum C_Q of each of the studied Zr_2CO_2 systems decreased gradually with increasing temperature. (Figure 6c)

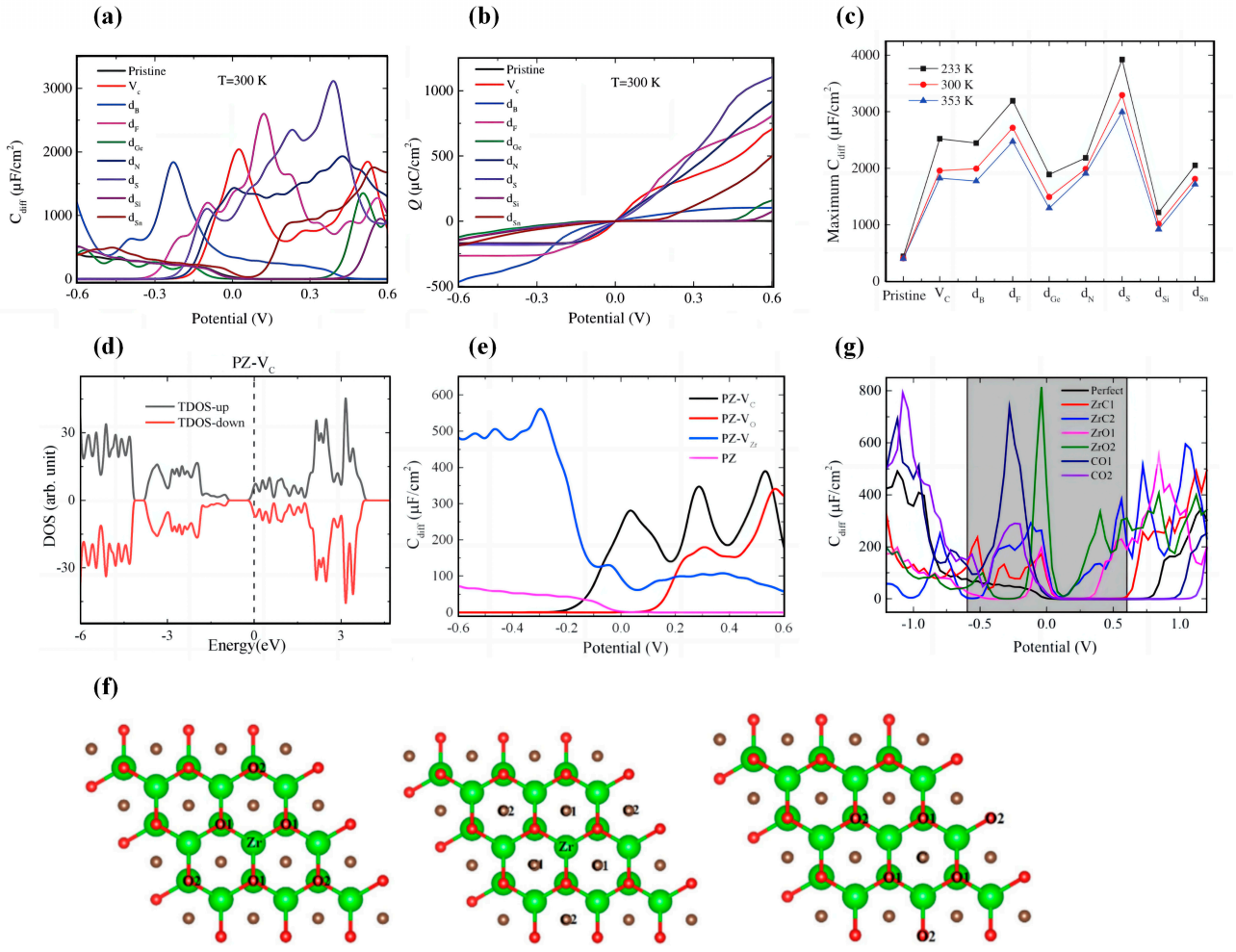

Figure 6. (**a**,**b**) C_Q and surface charge versus potential curves for the doped or vacant Zr_2CO_2. (**c**) The maximum C_Q of pristine Zr_2CO_2, Zr_2CO_2-V_C, and doped Zr_2CO_2 at different temperatures. (**d**) DOS of a C-vacant Zr_2CO_2 monolayer (PZ-V_C). (**e**) shows the C_Q versus potential of PZ-V_C, PZ-V_O, and PZ-V_{Zr}. (**f**) Schematic diagram of Zr_2CO_2 with different atomic exchange modifications. (**g**) C_Q versus potential plot for atomic exchanged Zr_2CO_2.

Li et al. investigated the effect of C, O, and Zr vacancies (V_C, V_O, V_{Zr}) on the C_Q of Zr_2CO_2 monolayers [124]. Their study shows that the introduction of atomic vacancies increases the maximum C_Q in the range of ±0.6 V. In particular, the maximum C_Q of PZ-VZr at positive bias is 586 μF/cm^2 (−0.30 V). The maximum C_Q of PZ-VC MXene under positive bias is 422 μF/cm^2 (0.53 V), while the maximum C_Q of PZ-VO MXene is 359 μF/cm^2 (0.57 V) (Figure 6d,e). Yin et al. investigated the C_Q of Zr_2CO_2 with an atomic exchange [125]. According to the plot of C_Q-V, they point out that, in the range of ±0.6 V, the C_Q of the pristine Zr_2CO_2 tends to be zero in positive bias, and in negative bias, the highest C_Q is 76.8 μF/cm^2. The highest C_Q is 737.1 μF/cm^2 in negative bias for the C-O1 exchanged system and 814.6 μF/cm^2 in negative bias for the Zr-O_2 exchanged system. The atomic exchange in Zr_2CO_2 greatly improves the top C_Q at negative bias in ±0.6 V. The Zr-O_2 exchanged system has the highest C_Q of 425.3 μF/cm^2 at 0 V (Figure 6f,g).

3.2.5. $Nb_{n+1}A_nT_x$

The first synthesized 2D niobium carbide was the thicker Nb_4C_3. The Nb_2C and Nb_3C_2 systems have an extremely high theoretical capacitance of Li atoms. Additionally, the surface termination has a considerable effect on the energy storage performance [126].

Xin et al. explored the C_Q properties of different thicknesses of $Nb_{n+1}C_n$ (n = 2, 3, 4) [127]. They noted that the C_Q values of all intrinsic niobium carbides were higher than that of functionalized ones in the positive bias voltage range. Except for Nb_5C_4, the other three niobium carbides have higher C_Q values at positive bias than at negative bias. The functionalized $Nb_{n+1}C_n$ shows a higher C_Q than the intrinsic system only at potentials below −0.4 V. In the positive bias range, functionalization causes a significant decrease in the C_Q of the system. To quantitatively compare the C_Q, they calculated the theoretical integrated C_Q of the positive and negative electrodes from 0 to 0.83 V and from −0.62 to 0 V, respectively. Their results illustrate that the C_Q of the intrinsic niobium carbide gradually decreases with the increasing number of layers in the positive potential region. For different thicknesses of functionalized $Nb_{n+1}C_n$ MXenes, the C_Q is smaller than the intrinsic state. The C_Q of intrinsic Nb_2C is up to 1828.4 F/g at the positive electrode and 1091.1 F/g at the negative electrode (Figure 7a–c).

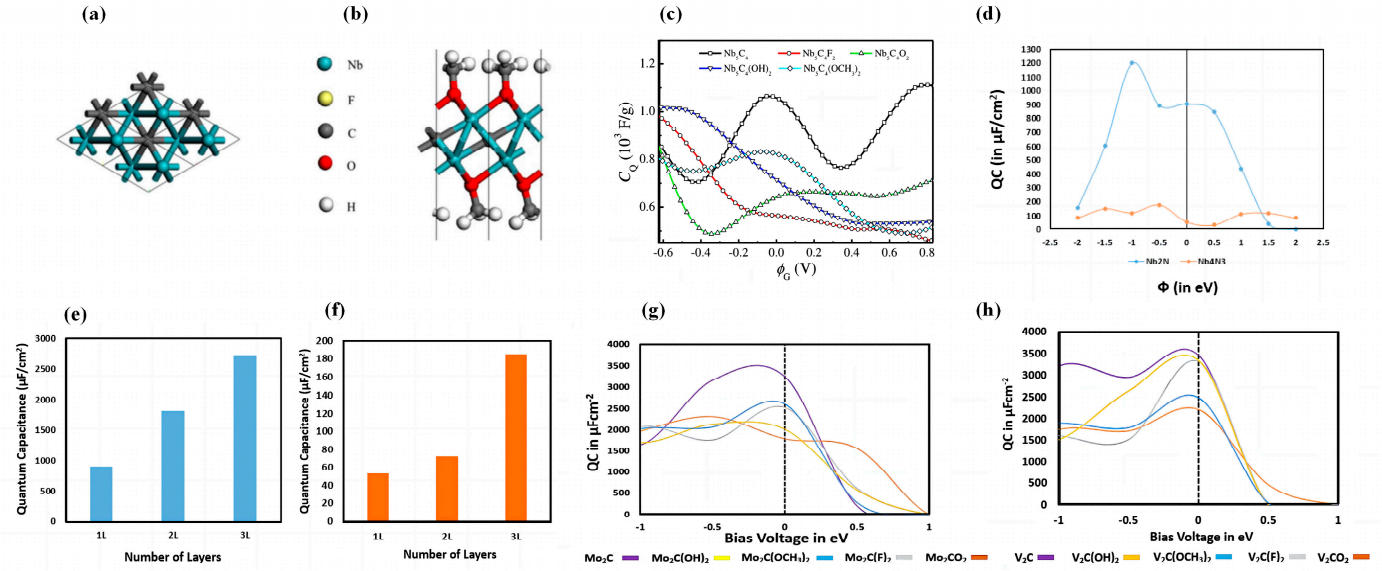

Figure 7. (**a**) Top view of Nb_2C structure. (**b**) Side view of $Nb_2C(OCH_3)_2$. (**c**) C_Q versus potential curves of Nb_5C_4 adsorbed with different functional groups. (**d**) Variation in C_Q for pristine unpolarized niobium nitride structures under bias voltage. (**e**,**f**) C_Q of multilayered Nb_2N and Nb_4N_3. (**g**,**h**) C_Q versus potential curves for functionalized Mo_2C and V_2C.

Transition metal nitrides, such as vanadium nitride, titanium nitride, and tungsten nitride, have been studied as electrode materials for EDLCs. It has been demonstrated that cobalt doping can increase the capacitance of niobium nitride. Bharti et al. calculated the C_Q of Nb_2N and Nb_4N_3 and investigated the effect of Co-doping on their C_Q [128]. Their calculations show that the C_Q value of Nb_2N is remarkably high (1196.28 μF/cm^2, −1 V) and the C_Q of Nb_4N_3 is much lower than that of Nb_2N. When they increased the number of layers of Nb_2N and Nb_4N_3, they found that the C_Q kept increasing with the more layer numbers. The C_Q of both Nb_4N_3 (Nb_4N_3-2Co) and Nb2N (Nb_2N-2Co) increase after Co-doping at the Fermi level, with the C_Q of Nb_2N-2Co reaching 1052.2 μF/cm^2 (Figure 7d–f).

3.2.6. Mo_2C and V_2C

Two-dimensional transition metal carbides (TMCs) have high melting points and good electrical conductivity and chemical stability [129–131]. With its excellent electrochemical properties, Mo_2C has been experimentally prepared as an electrode material for capacitors. In a experiment prepared by Lu et al., the capacitor with Mo_2C as the electrode material had a high specific capacitance and excellent cycling stability, and its performance was significantly better than most carbide-based asymmetric supercapacitors [132]. As early as 2015, it was shown that V_2CT_x could be used as the positive electrode of sodium ion capacitors [133]. The results of Ai et al.'s study show that the specific capacitance of V_2C in 1 M Na_2SO_4 is high (223.5 F/g) and the cycling stability is good (capacitance retention could be maintained at 94.7% after 5000 cycles) when the current density is 100 mA/g [134].

Bharti et al. discussed the C_Q of Mo_2C and V_2C [135]. They highlighted that the C_Q of intrinsic Mo_2C and V_2C reaches 3243.99 μF/cm^2 and 3465.51 μF/cm^2 at the Fermi level, respectively. In the positive potential range, the C_Q decreases rapidly and drops to 0. Similar to Nb_2N and Nb_4N_3, the C_Q of Mo_2C and V_2C enhances with the increasing number of layers. The C_Q values of both Mo_2C and V_2C at the Fermi energy decreased after O-functionalization. Similar to the pristine system, the O-functionalized V_2C and Mo_2C had higher C_Q at negative bias (Figure 7g,h).

3.3. Transition Metal Dichalcogenides (TMDs)

Transition metal-based materials are considered to have higher energy density than other materials [136–139]. Among them, transition metal dichalcogenides (TMDs) are a class of graphene-like structures that have been commonly used in terms of electrode materials for supercapacitors in recent years. Although TMDs usually store energy in the form of intercalation with alkali metals, they exhibit quantum effects that are reflected in their capacitive behavior.

MoS_2 is a typical representative of TMDs and exists in three main phases (2H, 3R, and 1T) with unique capacitive properties. Graphene-like MoS_2 materials have special structures, fast ionic conductivity, and high specific capacitance [140,141]. In addition, the electron correlation between Mo layers in the sandwich structure facilitates the carrier transport [142–144]. It is an excellent electrode material for supercapacitors and has attracted more and more attention.

MoS_2 was the subject of a comprehensive study by Xu et al. [145]. They first investigated the relationship between the C_Q and the potential of MoS_2 containing different dopants (where Ti, Au, Ag, Cu, and Al replace Mo atoms), single-vacancy V_{Mo}. Their results show that the C_Q of pristine MoS_2 is almost zero in the region near 0 V and increases at a higher voltage. For the C_Q of Al-doped MoS_2 and single-vacancy V_{Mo}, the local C_Q maxima near 0 V are 157.7 μF/cm^2 and 156.5 μF/cm^2, respectively. Subsequently, they observed the effect of Al doping on the C_Q in both pristine and single-vacant (VS) MoS_2 monolayers with different Al concentrations of 1.3%, 2.1%, 3.7%, and 8.3%. The C_Q value increases from 44.76 μF/cm^2 (0.17 V) to 227.85 μF/cm^2 (0.53 V) with the increase in doping concentration (Figure 8a–e). Secondly, they investigated the doped VS-MoS_2, where Ti, Au, Ag, Cu, and Al replace the S atoms. The C_Q increased in all systems except when doped with Ti, which is similar to that of S substitution in pristine MoS_2 (Figure 8f). Finally, they

calculated the local C_Q maxima of 200.89 μF/cm^2, 132.77 μF/cm^2, and 254.29 μF/cm^2 in B-, N-, and P-substituted S atoms in the B-, N-, and P-doped MoS_2 monolayer (doping concentration kept at 3.7%), respectively. At the Fermi level, the B-doped system had higher C_Q and a clear advantage in terms of positive potential (Figure 8g). Therefore, they continued to investigate the effect of B-doping concentration on C_Q. The C_Q value increased gradually with the increase of B-doping concentration.

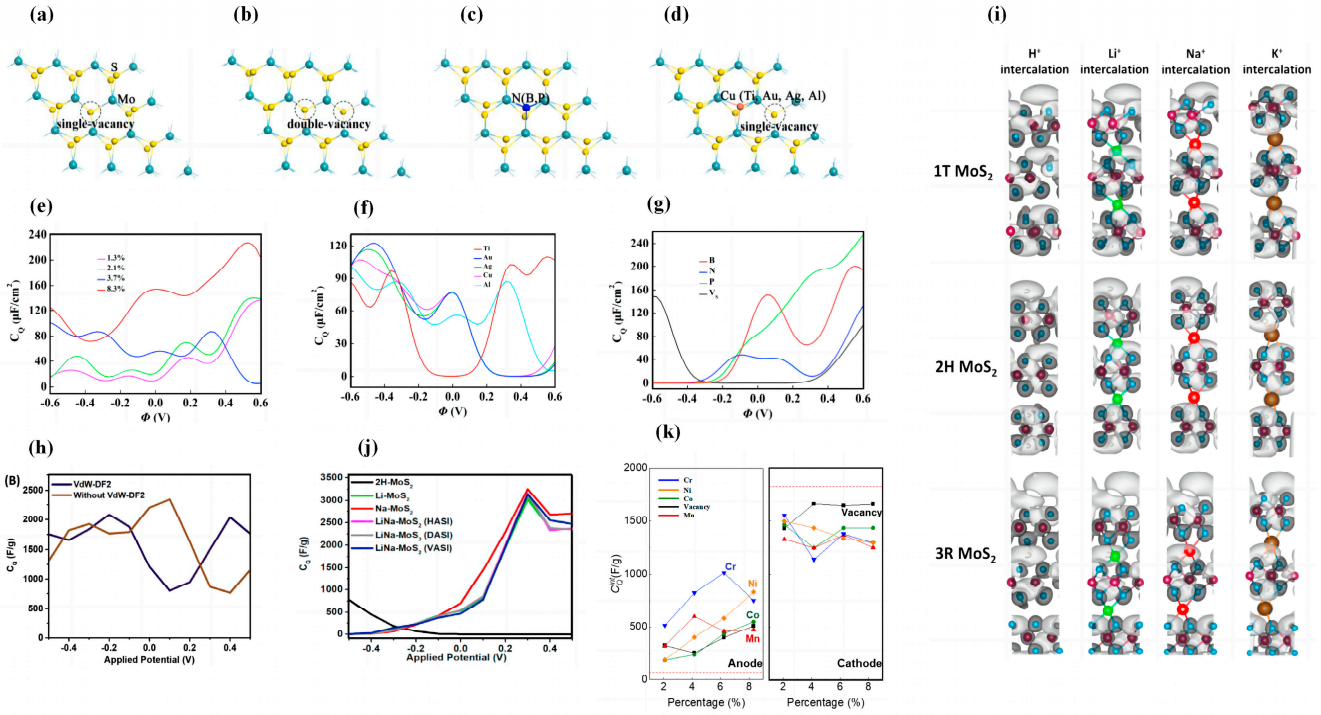

Figure 8. Structures of (**a**) single-vacant (VS) MoS_2 monolayer; (**b**) double-vacant (V_2S) MoS_2 monolayer; (**c**) B, N, P, Ti, Au, Ag, Cu, and Al-doped MoS_2 monolayer; (**d**) Ti, Au, Ag, Cu, and Al-doped VS-MoS_2 monolayer. (**e**) The plot of C_Q versus potential for VS-MoS_2 monolayers with Al substituted S atoms at different doping concentrations. (**f**) C_Q versus potential plot for VS-MoS_2 monolayers with Ti-, Au-, Ag-, Cu-, and Al-substituted S atoms. (**g**) The plot of C_Q versus potential for pristine MoS_2 monolayers with B-, N-, and P-substituted S atoms. (**h**) Plots of C_Q versus potential with and without vdW for three-layered 1T-phase MoS_2. (**i**) Plots of differential charge density for 1T, 2H, and 3R-phases MoS_2. (**j**) C_Q versus potential curves for Li^+ and Na^+ co-doped 2H phase MoS_2. (**k**) C_{int} of *h*-FeS for anode-like and cathode-like supercapacitors at different doping concentrations.

It is worth noting that MoS_2 should be considered as a van der Waals (vdW) 2D material. Biby et al. investigated the C_Q of multilayered MoS_2 with embedding and co-embedding in relation to vdW forces [146]. The C_Q of the three-layered 1T phases was as high as 2080 F/g, and the C_Q of 3R-MoS_2 was slightly higher than that of 2H-MoS_2 under negative bias. Subsequently, in their investigation on the effect of vdW forces on the C_Q, they pointed out that the absence of vdW forces increased the strength of the density of electric states. Thus, for 1T-MoS_2, the absence of vdW leads to a higher C_Q at positive bias, and in the case of 2H and 3R-MoS_2, the absence of vdW shifts the Fermi level, leading to a higher C_Q in the negative potential window. This finding also directly emphasizes the importance of vdW forces in the accurate calculation of 2D material properties (Figure 8h,i). Finally, they investigated the intercalation of cations (Li^+, Na^+, K^+ and H^+) in the three phases of MoS_2 and mixed Li^+ and Na^+ intercalation. They conclude that the C_Q of the 1T phase is increased near the Fermi level with Na^+ intercalation. Additionally, the 2H and 3R phases have a larger improvement, mainly in the positive bias voltage. There are three different intercalation modes in the case of mixed doping, and the C_Q values

of the co-intercalated system are higher than 2H Li-MoS_2 and close to 2H Na-MoS_2. The maximum C_Q of LiNa-MoS_2 (HASI) can reach 3163 F/g (Figure 8j) [146].

Irham et al. showed that the introduction of defects in h-FeS increased the C_Q at positive bias up to 2280 F/g, but the C_Q at negative bias decreased [147]. Cr-doped FeS has a maximum C_Q of 3076 F/g (0.6 V) at positive bias. *P*-type dopants (Co or Ni) do not significantly increase the C_Q in the positive voltage range. In their study of the integrated C_Q, they found that the C_{int} also changes nonlinearly with the doping concentration at positive bias, where the C_{int} can reach 1013 F/g with the Cr-doping concentration of 6.24%. They attribute the emergence of these nonlinear changes to the appearance of electronic off-domain states that hinder the increase of C_{int} (Figure 8k).

4. Conclusions

In this paper, we reviewed studies investigating the C_Q of 2D electrode materials through using theoretical calculations. In general, there are two solutions to enhance the performance of electrode materials for supercapacitors. One is to develop new electrode materials with higher performance, and the other is to modify the already found electrode materials, mainly by means of doping, adsorption, defects, atom exchange, etc. As far as the available studies are concerned, for graphene-like main group elements and compounds, all of the modification measures mentioned above can improve the C_Q of the electrode material. In contrast, in MXene materials, not all modification measures are able to improve the material performance. For example, the C_Q of functionalized Ti_3C_2 is not higher than that of the pristine structure. However, the introduction of functional groups during the preparation process is inevitable. Thus, it is necessary to investigate the C_Q of the functionalized MXenes to select the preparation precursors with the least impact on energy storage performance. There are not many studies on C_Q in transition metal-based supercapacitor electrode materials. Most TM-based materials are considered as pseudocapacitance supercapacitor materials. However, both pseudocapacitance and electric double-layer processes exist in such supercapacitors. So calculating the C_Q of TM-based electrode materials can lead to a more accurate prediction of the theoretical capacitance and provide more possibilities for the development of supercapacitors.

Nowadays, theoretical calculation plays an important role in scientific research. On the one hand, theoretical calculations can help interpret the results of existing experimental phenomena, and on the other hand, they facilitate the prediction and development of new materials. Most of the current studies on the theoretical calculation of electrode materials for supercapacitors focus on predicting new materials. Although the high performance of electrode materials has been calculated theoretically, there are still great difficulties in the preparation process. In addition, the current research only pertains to the electrode part, and the performance of the whole capacitor has not been completely considered. Further research should pay more attention to the feasibility and stability of material modification. Secondly, various variables that may cause influence should be fully considered so that the theoretical prediction is closer to the real situation. And thirdly, the amount of attention given to the overall performance and process of supercapacitors should be improved. With the advancement of science and technology, theoretical calculations have become more accurate and fast. This also provides us with a more thorough explanation of supercapacitor performance and greater feasibility for designing functional materials with various properties. We expect that theoretical calculations will provide a greater contribution to the development of supercapacitors.

Funding: This work was funded by the Natural Science Foundation of China under No. 12204065; the Natural Science Foundation of Jilin Province (Grant Nos. YDZJ202201ZYTS576 and 20220508020RC), the 13th and 14th Five-year Planning Project of Jilin Provincial Education Department Foundation (Grant Nos. JJKH20200828KJ and JJKH20220836KJ), the Natural Science Foundation (Grant Nos. 001010, and 003179), and the PhD Starting Scientific Research Funding Project (No. 00300200360) of Changchun Normal University.

Data Availability Statement: No new data were created or analyzed in this study. Data sharing is not applicable to this article.

Conflicts of Interest: The authors declare no conflict of interest.

References

1. Huang, Y.; Zhu, M.; Huang, Y.; Pei, Z.; Li, H.; Wang, Z.; Xue, Q.; Zhi, C. Multifunctional Energy Storage and Conversion Devices. *Adv. Mater.* **2016**, *28*, 8344–8364. [CrossRef]
2. Naguib, M.; Mochalin, V.N.; Barsoum, M.W.; Gogotsi, Y. 25th anniversary article: MXenes: A new family of two-dimensional materials. *Adv. Mater.* **2014**, *26*, 992–1005. [CrossRef]
3. Yu, Z.; Tetard, L.; Zhai, L.; Thomas, J. Supercapacitor electrode materials: Nanostructures from 0 to 3 dimensions. *Energy Environ. Sci.* **2015**, *8*, 702–730. [CrossRef]
4. Vangari, M.; Pryor, T.; Jiang, L. Supercapacitors: Review of Materials and Fabrication Methods. *J. Energ. Eng.* **2013**, *139*, 72–79. [CrossRef]
5. Raza, W.; Ali, F.; Raza, N.; Luo, Y.; Kim, K.-H.; Yang, J.; Kumar, S.; Mehmood, A.; Kwon, E.E. Recent advancements in supercapacitor technology. *Nano Energy* **2018**, *52*, 441–473. [CrossRef]
6. Libich, J.; Máca, J.; Vondrák, J.; Čech, O.; Sedlaříková, M. Supercapacitors: Properties and applications. *J. Energy Storage* **2018**, *17*, 224–227. [CrossRef]
7. Yang, W.; Ni, M.; Ren, X.; Tian, Y.; Li, N.; Su, Y.; Zhang, X. Graphene in Supercapacitor Applications. *Curr. Opin. Colloid. Interface Sci.* **2015**, *20*, 416–428. [CrossRef]
8. Najib, S.; Erdem, E. Current progress achieved in novel materials for supercapacitor electrodes: Mini review. *Nanoscale Adv.* **2019**, *1*, 2817–2827. [CrossRef]
9. Yin, X.; Zhang, J.; Yang, L.; Xiao, W.; Zhou, L.; Tang, Y.; Yang, W. Carbon electrodes with ionophobic characteristics in organic electrolyte for high-performance electric double-layer capacitors. *Sci. China Chem.* **2021**, *65*, 383–390. [CrossRef]
10. Schütter, C.; Pohlmann, S.; Balducci, A. Industrial Requirements of Materials for Electrical Double Layer Capacitors: Impact on Current and Future Applications. *Adv. Energy Mater.* **2019**, *9*, 00334. [CrossRef]
11. Zhan, C.; Neal, J.; Wu, J.; Jiang, D.-E. Quantum Effects on the Capacitance of Graphene-Based Electrodes. *J. Phys. Chem. C* **2015**, *119*, 22297–22303. [CrossRef]
12. Paek, E.; Pak, A.J.; Kweon, K.E.; Hwang, G.S. On the Origin of the Enhanced Supercapacitor Performance of Nitrogen-Doped Graphene. *J. Phys. Chem. C* **2013**, *117*, 5610–5616. [CrossRef]
13. Pak, A.J.; Paek, E.; Hwang, G.S. Relative contributions of quantum and double layer capacitance to the supercapacitor performance of carbon nanotubes in an ionic liquid. *Phys. Chem. Chem. Phys.* **2013**, *15*, 19741–19747. [CrossRef]
14. Yang, G.M.; Zhang, H.Z.; Fan, X.F.; Zheng, W.T. Density Functional Theory Calculations for the Quantum Capacitance Performance of Graphene-Based Electrode Material. *J. Phys. Chem. C* **2015**, *119*, 6464–6470. [CrossRef]
15. Paek, E.; Pak, A.J.; Hwang, G.S. Curvature Effects on the Interfacial Capacitance of Carbon Nanotubes in an Ionic Liquid. *J. Phys. Chem. C* **2013**, *117*, 23539–23546. [CrossRef]
16. Paek, E.; Pak, A.J.; Hwang, G.S. A Computational Study of the Interfacial Structure and Capacitance of Graphene in [BMIM][PF_6] Ionic Liquid. *J. Electrochem. Soc.* **2012**, *160*, A1–A10. [CrossRef]
17. Yu, G.L.; Jalil, R.; Belle, B.; Mayorov, A.S.; Blake, P.; Schedin, F.; Morozov, S.V.; Ponomarenko, L.A.; Chiappini, F.; Wiedmann, S.; et al. Interaction phenomena in graphene seen through quantum capacitance. *Proc. Natl. Acad. Sci. USA* **2013**, *110*, 3282–3286. [CrossRef]
18. Luryi, S. Quantum capacitance devices. *Appl. Phys. Lett.* **1988**, *52*, 501–503. [CrossRef]
19. John, D.L.; Castro, L.C.; Pulfrey, D.L. Quantum capacitance in nanoscale device modeling. *J. Appl. Phys* **2004**, *96*, 5180–5184. [CrossRef]
20. Zhang, L.; Huang, K.; Wen, P.; Wang, J.; Yang, G.; Liu, D.; Lin, Z.; Lian, C.; Liu, H.; Zheng, S.; et al. Tailoring the defects of two-dimensional borocarbonitride nanomesh for high energy density micro-supercapacitor. *Energy Stor. Mater.* **2021**, *42*, 430–437. [CrossRef]
21. Lu, X.; Wang, C.; Favier, F.; Pinna, N. Electrospun Nanomaterials for Supercapacitor Electrodes: Designed Architectures and Electrochemical Performance. *Adv. Energy Mater.* **2017**, *7*, 1601301. [CrossRef]
22. Poudel, M.B.; Kim, H.J. Confinement of Zn-Mg-Al-layered double hydroxide and α-Fe_2O_3 nanorods on hollow porous carbon nanofibers: A free-standing electrode for solid-state symmetric supercapacitors. *Chem. Eng J.* **2022**, *429*, 132345. [CrossRef]
23. He, P.; Chen, S. Vertically Oriented Graphene Nanosheets for Electrochemical Energy Storage. *ChemElectroChem* **2021**, *8*, 783–797. [CrossRef]
24. Bokhari, S.W.; Siddique, A.H.; Sherrell, P.C.; Yue, X.; Karumbaiah, K.M.; Wei, S.; Ellis, A.V.; Gao, W. Advances in graphene-based supercapacitor electrodes. *Energy Rep.* **2020**, *6*, 2768–2784. [CrossRef]
25. Frackowiak, E. Carbon materials for supercapacitor application. *Phys. Chem. Chem. Phys.* **2007**, *9*, 1774–1785. [CrossRef]
26. Zhang, L.L.; Zhao, X.S. Carbon-based materials as supercapacitor electrodes. *Chem. Soc. Rev.* **2009**, *38*, 252031. [CrossRef]
27. Borenstein, A.; Hanna, O.; Attias, R.; Luski, S.; Brousse, T.; Aurbach, D. Carbon-based composite materials for supercapacitor electrodes: A review. *J. Mater. Chem. A* **2017**, *5*, 12653–12672. [CrossRef]

28. Hirunsit, P.; Liangruksa, M.; Khanchaitit, P. Electronic structures and quantum capacitance of monolayer and multilayer graphenes influenced by Al, B, N and P doping, and monovacancy: Theoretical study. *Carbon* **2016**, *108*, 7–20. [CrossRef]
29. Kopp, T.; Mannhart, J. Calculation of the capacitances of conductors: Perspectives for the optimization of electronic devices. *J. Appl. Phys.* **2009**, *106*, 064504. [CrossRef]
30. Lin, J.; Yu, T.; Han, F.; Yang, G. Computational predictions of two-dimensional anode materials of metal-ion batteries. *Wiley. Interdiscip. Rev. Comput. Mol. Sci.* **2020**, *10*, 147310. [CrossRef]
31. Malko, D.; Neiss, C.; Vines, F.; Gorling, A. Competition for graphene: Graphynes with direction-dependent Dirac cones. *Phys. Rev. Lett.* **2012**, *108*, 086804. [CrossRef] [PubMed]
32. Tiwari, S.K.; Sahoo, S.; Wang, N.; Huczko, A. Graphene research and their outputs: Status and prospect. *J. Sci. Adv. Mater. Devices* **2020**, *5*, 10–29. [CrossRef]
33. Xia, J.; Chen, F.; Li, J.; Tao, N. Measurement of the quantum capacitance of graphene. *Nat. Nanotechnol.* **2009**, *4*, 505–509. [CrossRef]
34. Jeong, H.M.; Lee, J.W.; Shin, W.H.; Choi, Y.J.; Shin, H.J.; Kang, J.K.; Choi, J.W. Nitrogen-doped graphene for high-performance ultracapacitors and the importance of nitrogen-doped sites at basal planes. *Nano Lett.* **2011**, *11*, 2472–2477. [CrossRef] [PubMed]
35. Kim, W.; Joo, J.B.; Kim, N.; Oh, S.; Kim, P.; Yi, J. Preparation of nitrogen-doped mesoporous carbon nanopipes for the electrochemical double layer capacitor. *Carbon* **2009**, *47*, 1407–1411. [CrossRef]
36. Li, W.; Chen, D.; Li, Z.; Shi, Y.; Wan, Y.; Wang, G.; Jiang, Z.; Zhao, D. Nitrogen-containing carbon spheres with very large uniform mesopores: The superior electrode materials for EDLC in organic electrolyte. *Carbon* **2007**, *45*, 1757–1763. [CrossRef]
37. Seredych, M.; Hulicova-Jurcakova, D.; Lu, G.Q.; Bandosz, T.J. Surface functional groups of carbons and the effects of their chemical character, density and accessibility to ions on electrochemical performance. *Carbon* **2008**, *46*, 1475–1488. [CrossRef]
38. Lota, G.; Frackowiak, E. Pseudocapacitance Effects for Enhancement of Capacitor Performance. *Fuel Cells* **2010**, *10*, 848–855. [CrossRef]
39. Qiu, Y.; Zhang, X.; Yang, S. High performance supercapacitors based on highly conductive nitrogen-doped graphene sheets. *Phys. Chem. Chem. Phys.* **2011**, *13*, 125548. [CrossRef]
40. Paraknowitsch, J.P.; Zhang, J.; Su, D.; Thomas, A.; Antonietti, M. Ionic liquids as precursors for nitrogen-doped graphitic carbon. *Adv. Mater.* **2010**, *22*, 87–92. [CrossRef]
41. Hulicova-Jurcakova, D.; Kodama, M.; Shiraishi, S.; Hatori, H.; Zhu, Z.H.; Lu, G.Q. Nitrogen-Enriched Nonporous Carbon Electrodes with Extraordinary Supercapacitance. *Adv. Funct. Mater.* **2009**, *19*, 1800–1809. [CrossRef]
42. Zhang, L.L.; Zhao, X.; Ji, H.; Stoller, M.D.; Lai, L.; Murali, S.; McDonnell, S.; Cleveger, B.; Wallace, R.M.; Ruoff, R.S. Nitrogen doping of graphene and its effect on quantum capacitance, and a new insight on the enhanced capacitance of N-doped carbon. *Energy Environ. Sci.* **2012**, *5*, 9618–9625. [CrossRef]
43. Mousavi-Khoshdel, S.M.; Targholi, E. Exploring the effect of functionalization of graphene on the quantum capacitance by first principle study. *Carbon* **2015**, *89*, 148–160. [CrossRef]
44. Chen, L.; Li, X.; Ma, C.; Wang, M.; Zhou, J. Interaction and Quantum Capacitance of Nitrogen/Sulfur Co-Doped Graphene: A Theoretical Calculation. *J. Phys. Chem. C* **2017**, *121*, 18344–18350. [CrossRef]
45. Hu, R.; Shang, J. Quantum capacitance of transition metal and nitrogen co-doped graphenes as supercapacitors electrodes: A DFT study. *Appl. Surf. Sci.* **2019**, *496*, 143659. [CrossRef]
46. Wang, M.; Chen, L.; Zhou, J.; Xu, L.; Li, X.; Li, L.; Li, X. First-principles calculation of quantum capacitance of metals doped graphenes and nitrogen/metals co-doped graphenes: Designing strategies for supercapacitor electrodes. *J. Mater. Sci.* **2018**, *54*, 483–492. [CrossRef]
47. Song, C.; Wang, J.; Meng, Z.; Hu, F.; Jian, X. Density Functional Theory Calculations of the Quantum Capacitance of Graphene Oxide as a Supercapacitor Electrode. *Chemphyschem* **2018**, *19*, 1579–1583. [CrossRef]
48. Sruthi, T.; Kartick, T. Route to achieving enhanced quantum capacitance in functionalized graphene based supercapacitor electrodes. *J. Phys. Condens. Matter.* **2019**, *31*, 475502. [CrossRef]
49. Xu, Q.; Yang, G.; Fan, X.; Zheng, W. Improving the Quantum Capacitance of Graphene-Based Supercapacitors by the Doping and Co-Doping: First-Principles Calculations. *ACS Omega* **2019**, *4*, 13209–13217. [CrossRef]
50. Zhang, B.; Peng, Z.; Song, L.; Wu, X.; Fu, X. Computational screening toward quantum capacitance of transition-metals and vacancy doped/co-doped graphene as electrode of supercapacitors. *Electrochim. Acta* **2021**, *385*, 138432. [CrossRef]
51. Sruthi, T.; Tarafder, K. Enhancement of quantum capacitance by chemical modification of graphene supercapacitor electrodes: A study by first principles. *Bull. Mater. Sci.* **2019**, *42*, 257–263. [CrossRef]
52. Cui, G.-Y.; Yi, Z.-L.; Su, F.-Y.; Chen, C.-M.; Han, P.-D. A DFT study of the effect of stacking on the quantum capacitance of bilayer graphene materials. *New Carbon Mater.* **2021**, *36*, 1062–1070. [CrossRef]
53. Zhou, Q.; Ju, W.; Yong, Y.; Zhang, Q.; Liu, Y.; Li, J. Effect of the N/P/S and transition-metal co-doping on the quantum capacitance of supercapacitor electrodes based on mono- and multilayer graphene. *Carbon* **2020**, *170*, 368–379. [CrossRef]
54. Zeng, W.; Zhang, Y.; Liu, X.; Qi, L.; Kang, W.; Fang, L.; Zhou, M. B/N-doped graphdiyne as superior supercapacitor electrode with record high quantum capacitance. *Appl. Surf. Sci.* **2020**, *523*, 146468. [CrossRef]
55. Nawaz, S.; Tahir, M. Quantum capacitance in monolayers of silicene and related buckled materials. *Phys. E Low Dimens. Syst. Nanostruct.* **2016**, *76*, 169–172. [CrossRef]

56. Yang, G.M.; Xu, Q.; Fan, X.; Zheng, W.T. Quantum Capacitance of Silicene-Based Electrodes from First-Principles Calculations. *J. Phys. Chem. C* **2018**, *122*, 1903–1912. [CrossRef]
57. Momeni, M.J.; Mousavi-Khoshdel, M.; Leisegang, T. Exploring the performance of pristine and defective silicene and silicene-like XSi_3 (X = Al, B, C, N, P) sheets as supercapacitor electrodes: A density functional theory calculation of quantum capacitance. *Phys. E Low Dimens. Syst. Nanostruct.* **2020**, *124*, 114290. [CrossRef]
58. Xu, Q.; Yang, G.M.; Fan, X.; Zheng, W.T. Adsorption of metal atoms on silicene: Stability and quantum capacitance of silicene-based electrode materials. *Phys. Chem. Chem. Phys.* **2019**, *21*, 4276–4285. [CrossRef]
59. Liu, C.-C.; Jiang, H.; Yao, Y. Low-energy effective Hamiltonian involving spin-orbit coupling in silicene and two-dimensional germanium and tin. *Phys. Rev. B* **2011**, *84*, 195430. [CrossRef]
60. Kaloni, T.P. Tuning the Structural, Electronic, and Magnetic Properties of Germanene by the Adsorption of 3d Transition Metal Atoms. *J. Phys. Chem. C* **2014**, *118*, 25200–25208. [CrossRef]
61. Xu, Q.; Si, X.; She, W.H.; Yang, G.M.; Fan, X.; Zheng, W.T. First-Principles Calculation of Optimizing the Performance of Germanene-Based Supercapacitors by Vacancies and Metal Atoms. *J. Phys. Chem. C* **2020**, *124*, 12346–12358. [CrossRef]
62. Zhang, L.; Bampoulis, P.; Rudenko, A.N.; Yao, Q.; van Houselt, A.; Poelsema, B.; Katsnelson, M.I.; Zandvliet, H.J. Structural and Electronic Properties of Germanene on MoS_2. *Phys. Rev. Lett.* **2016**, *116*, 256804. [CrossRef] [PubMed]
63. Liu, N.; Bo, G.; Liu, Y.; Xu, X.; Du, Y.; Dou, S.X. Recent Progress on Germanene and Functionalized Germanene: Preparation, Characterizations, Applications, and Challenges. *Small* **2019**, *15*, 1805147. [CrossRef]
64. Zhuang, J.; Gao, N.; Li, Z.; Xu, X.; Wang, J.; Zhao, J.; Dou, S.X.; Du, Y. Cooperative Electron-Phonon Coupling and Buckled Structure in Germanene on Au(111). *ACS Nano* **2017**, *11*, 3553–3559. [CrossRef] [PubMed]
65. Qin, Z.; Pan, J.; Lu, S.; Shao, Y.; Wang, Y.; Du, S.; Gao, H.J.; Cao, G. Direct Evidence of Dirac Signature in Bilayer Germanene Islands on Cu(111). *Adv. Mater.* **2017**, *29*, 1606046. [CrossRef] [PubMed]
66. Wang, W.; Uhrberg, R.I.G. Investigation of the atomic and electronic structures of highly ordered two-dimensional germanium on Au(111). *Phys. Rev. Mater.* **2017**, *1*, 074002. [CrossRef]
67. Zhuang, J.; Liu, C.; Zhou, Z.; Casillas, G.; Feng, H.; Xu, X.; Wang, J.; Hao, W.; Wang, X.; Dou, S.X.; et al. Dirac Signature in Germanene on Semiconducting Substrate. *Adv. Sci. (Weinh)* **2018**, *5*, 180–207. [CrossRef]
68. Zhou, Q.; Ju, W.; Yong, Y.; Liu, Y.; Li, J. Quantum capacitance of supercapacitor electrodes based on germanene influenced by vacancy and co-doping: A first-principles study. *Comput. Mater. Sci.* **2021**, *188*, 110131. [CrossRef]
69. Si, X.; She, W.; Xu, Q.; Yang, G.; Li, Z.; Wang, S.; Luan, J. First-Principles Density Functional Theory Study of Modified Germanene-Based Electrode Materials. *Materials* **2021**, *15*, 103. [CrossRef]
70. Abbasi, A.; Sardroodi, J.J. The adsorption of sulfur trioxide and ozone molecules on stanene nanosheets investigated by DFT: Applications to gas sensor devices. *Phys. E Low Dimens. Syst. Nanostruct.* **2019**, *108*, 382–390. [CrossRef]
71. Zhang, A.; Yang, H.; Liu, Q.; Li, W.; Wang, Y. DFT insights into the adsorption properties of toxic gas molecules on pure and transition metal embedded stanene monolayers: Towards gas sensor devices. *Synth. Met.* **2020**, *266*, 116441. [CrossRef]
72. Nagarajan, V.; Chandiramouli, R. Adsorption behavior of NH_3 and NO_2 molecules on stanene and stanane nanosheets—A density functional theory study. *Chem. Phys. Lett.* **2018**, *695*, 162–169. [CrossRef]
73. Sahoo, S.K.; Wei, K.H. A Perspective on Recent Advances in 2D Stanene Nanosheets. *Adv. Mater. Interfaces* **2019**, *6*, 00752. [CrossRef]
74. Shaidu, Y.; Akin-Ojo, O. First principles predictions of superconductivity in doped stanene. *Comput. Mater. Sci.* **2016**, *118*, 11–15. [CrossRef]
75. Evazzade, I.; Roknabadi, M.R.; Morshedloo, T.; Modarresi, M.; Mogulkoc, Y.; Nemati Far, H. Semimetal behavior of bilayer stanene. *Phys. E Low Dimens. Syst. Nanostruct.* **2017**, *89*, 155–159. [CrossRef]
76. Zhou, Q.; Wang, L.; Ju, W.; Yong, Y.; Wu, S.; Cai, S.; Li, P. Quantum capacitance of vacancy-defected and co-doped stanene for supercapacitor electrodes: A theoretical study. *Electrochim. Acta* **2022**, *433*, 141261. [CrossRef]
77. Zhou, Q.; Wang, L.; Ju, W.; Miao, H.; Ye, S.; Liu, Y. Influence of the co-doping and line-doping on the quantum capacitance of stanene for supercapacitor electrodes. *Chem. Phys. Lett.* **2022**, *808*, 140123. [CrossRef]
78. Zhong, H.-X.; Gao, S.; Shi, J.-J.; Yang, L. Quasiparticle band gaps, excitonic effects, and anisotropic optical properties of the monolayer distorted1Tdiamond-chain structuresReS_2 and$ReSe_2$. *Phys. Rev. B* **2015**, *92*, 115438. [CrossRef]
79. Ramasubramaniam, A. Large excitonic effects in monolayers of molybdenum and tungsten dichalcogenides. *Phys. Rev. B* **2012**, *86*, 115409. [CrossRef]
80. Cheng, T.; Lang, H.; Li, Z.; Liu, Z.; Liu, Z. Anisotropic carrier mobility in two-dimensional materials with tilted Dirac cones: Theory and application. *Phys. Chem. Chem. Phys.* **2017**, *19*, 23942–23950. [CrossRef]
81. Kolavada, H.; Singh, S.; Lukačević, I.; Gajjar, P.N.; Gupta, S.K. Quantum capacitance of multi-layered δ-6 borophene: A DFT study. *Electrochim. Acta* **2023**, *439*, 141589. [CrossRef]
82. Chen, X.; Wang, L.; Wu, Y.; Gao, H.; Wu, Y.; Qin, G.; Wu, Z.; Han, Y.; Xu, S.; Han, T.; et al. Probing the electronic states and impurity effects in black phosphorus vertical heterostructures. *2D Mater.* **2016**, *3*, 015012. [CrossRef]
83. Chen, X.; Xu, G.; Ren, X.; Li, Z.; Qi, X.; Huang, K.; Zhang, H.; Huang, Z.; Zhong, J. A black/red phosphorus hybrid as an electrode material for high-performance Li-ion batteries and supercapacitors. *J. Mater. Chem. A* **2017**, *5*, 6581–6588. [CrossRef]
84. Batmunkh, M.; Bat-Erdene, M.; Shapter, J.G. Phosphorene and Phosphorene-Based Materials—Prospects for Future Applications. *Adv. Mater.* **2016**, *28*, 8586–8617. [CrossRef]

85. Vishnoi, P.; Rajesh, S.; Manjunatha, S.; Bandyopadhyay, A.; Barua, M.; Pati, S.K.; Rao, C.N.R. Doping Phosphorene with Holes and Electrons through Molecular Charge Transfer. *Chemphyschem* **2017**, *18*, 2985–2989. [CrossRef]
86. Huang, Z.; Wu, Y.; Qi, X.; He, C.; Ren, X.; Zhong, J. Electronic and Magnetic Properties of Monolayer and Bilayer Phosphorene Doped with Transition-Metal Atoms. *Phys. Status Solidi. B* **2018**, *255*, 1700370. [CrossRef]
87. Zu, L.; Gao, X.; Lian, H.; Li, C.; Liang, Q.; Liang, Y.; Cui, X.; Liu, Y.; Wang, X.; Cui, X. Electrochemical prepared phosphorene as a cathode for supercapacitors. *J. Alloys Compd.* **2019**, *770*, 26–34. [CrossRef]
88. Ramesh, A.; Mir, A. Influence of heteroatom doping on the quantum capacitance of phosphorene supercapacitors. *J. Energy Storage* **2022**, *56*, 106013. [CrossRef]
89. Kessler, F.K.; Zheng, Y.; Schwarz, D.; Merschjann, C.; Schnick, W.; Wang, X.; Bojdys, M.J. Functional carbon nitride materials—Design strategies for electrochemical devices. *Nat. Rev. Mater. JCR* **2017**, *2*, 17030. [CrossRef]
90. Zhao, Z.; Sun, Y.; Dong, F. Graphitic carbon nitride based nanocomposites: A review. *Nanoscale* **2015**, *7*, 15–37. [CrossRef]
91. Liu, A.Y.; Wentzcovitch, R.M. Stability of carbon nitride solids. *Phys. Rev. B Condens. Matter.* **1994**, *50*, 10362–10365. [CrossRef] [PubMed]
92. Chen, X.; Xu, W.; Jin, J.; Wang, P.; Song, B.; He, P. Effect of B and O doping on the electronic structure and quantum capacitance of carbon nitride monolayers using first-principles calculations. *J. Appl. Phys.* **2021**, *129*, 174301. [CrossRef]
93. Majdi, A.; Kadhim Wadday, A.; Sabri Abbas, Z.; Kadhim, M.M.; Mahdi Rheima, A.; Barzan, M.; Haitham Alattia, L.; Hachim, S.K.; Abdul Hadi, M. Quantum capacitance of iron metal doped boron carbide monolayer-based for supercapacitors electrodes: A DFT study. *Inorg. Chem. Commun.* **2023**, *150*, 110480. [CrossRef]
94. Naguib, M.; Kurtoglu, M.; Presser, V.; Lu, J.; Niu, J.; Heon, M.; Hultman, L.; Gogotsi, Y.; Barsoum, M.W. Two-dimensional nanocrystals produced by exfoliation of Ti_3AlC_2. *Adv. Mater.* **2011**, *23*, 4248–4253. [CrossRef]
95. Zhan, X.; Si, C.; Zhou, J.; Sun, Z. MXene and MXene-based composites: Synthesis, properties and environment-related applications. *Nanoscale Horiz.* **2020**, *5*, 235–258. [CrossRef]
96. Shuck, C.E.; Sarycheva, A.; Anayee, M.; Levitt, A.; Zhu, Y.; Uzun, S.; Balitskiy, V.; Zahorodna, V.; Gogotsi, O.; Gogotsi, Y. Scalable Synthesis of $Ti_3C_2T_x$ MXene. *Adv. Eng. Mater.* **2020**, *22*, 01241. [CrossRef]
97. Li, X.; Wang, C.; Cao, Y.; Wang, G. Functional MXene Materials: Progress of Their Applications. *Chem. Asian J.* **2018**, *13*, 2742–2757. [CrossRef]
98. Hu, T.; Yang, J.; Wang, X. Carbon vacancies in Ti_2CT_2 MXenes: Defects or a new opportunity? *Phys. Chem. Chem. Phys.* **2017**, *19*, 31773–31780. [CrossRef]
99. Cheng, Y.-W.; Dai, J.-H.; Zhang, Y.-M.; Song, Y. Transition metal modification and carbon vacancy promoted Cr_2CO_2(MXenes): A new opportunity for a highly active catalyst for the hydrogen evolution reaction. *J. Mater. Chem. A* **2018**, *6*, 20956–20965. [CrossRef]
100. Er, D.; Li, J.; Naguib, M.; Gogotsi, Y.; Shenoy, V.B. Ti_3C_2 MXene as a high capacity electrode material for metal (Li, Na, K, Ca) lon batteries. *ACS Appl. Mater. Interfaces* **2014**, *6*, 11173–11179. [CrossRef]
101. Lipatov, A.; Alhabeb, M.; Lukatskaya, M.R.; Boson, A.; Gogotsi, Y.; Sinitskii, A. Effect of Synthesis on Quality, Electronic Properties and Environmental Stability of Individual Monolayer Ti_3C_2MXene Flakes. *Adv. Electron. Mater.* **2016**, *2*, 1600255. [CrossRef]
102. Si, X.; Xu, Q.; Lin, J.; Yang, G. Quantum capacitance modulation of MXenes by metal atoms adsorption. *Appl. Surf. Sci.* **2023**, *618*, 156586. [CrossRef]
103. Bafekry, A.; Nguyen, C.V.; Stampfl, C.; Akgenc, B.; Ghergherehchi, M. Oxygen Vacancies in the Single Layer of Ti_2CO_2 MXene: Effects of Gating Voltage, Mechanical Strain, and Atomic Impurities. *Phys. Status Solidi B* **2020**, *257*, 2000343. [CrossRef]
104. Su, X.; Guo, R.-G.; Xu, S.; Wang, S.-J.; Li, X.-H.; Cui, H.-L. Influence of O-vacancy concentration on the structural, electronic properties and quantum capacitance of monolayer Ti_2CO_2: A first-principles study. *Vacuum* **2022**, *196*, 110740. [CrossRef]
105. Li, X.-H.; Liu, M.-Z.; Tan, X.-M.; Su, X.; Guo, R.-G.; Zhang, R.-Z.; Cui, H.-L. Influence of C-vacancy-line defect on electronic and optical properties and quantum capacitance of Ti_2CO_2 MXene: A first-principles study. *J. Phys. Chem. Solids* **2023**, *176*, 111254. [CrossRef]
106. Li, X.-H.; Li, S.-S.; Cui, X.-H.; Zhang, R.-Z.; Cui, H.-L. First-principle study of electronic properties and quantum capacitance of lithium adsorption on pristine and vacancy-defected O-functionalized Ti_2C MXene. *Appl. Surf. Sci.* **2021**, *563*, 150264. [CrossRef]
107. Kumar, S.; Schwingenschlögl, U. Thermoelectric performance of functionalized Sc_2C MXenes. *Phys. Rev. B* **2016**, *94*, 035405. [CrossRef]
108. Ma, Z.; Hu, Z.; Zhao, X.; Tang, Q.; Wu, D.; Zhou, Z.; Zhang, L. Tunable Band Structures of Heterostructured Bilayers with Transition-Metal Dichalcogenide and MXene Monolayer. *J. Phys. Chem. C* **2014**, *118*, 5593–5599. [CrossRef]
109. Cui, X.-H.; Li, X.-H.; Jin, X.-J.; Zhang, R.-Z.; Cui, H.-L.; Yan, H.-T. First-principles study on the effect of atomic swap on the electronic properties and quantum capacitance of Sc_2CF_2 monolayer. *Vacuum* **2022**, *204*, 111371. [CrossRef]
110. Cui, X.-H.; Li, X.-H.; Zhang, R.-Z.; Cui, H.-L.; Yan, H.-T. Theoretical insight into the electronic, optical, and photocatalytic properties and quantum capacitance of Sc_2CT_2 (T = F, P, Cl, Se, Br, O, Si, S, OH) MXenes. *Vacuum* **2023**, *207*, 111615. [CrossRef]
111. Cui, X.-H.; Li, X.-H.; Li, S.-S.; Cui, H.-L. The effect of vacancy defect on quantum capacitance, electronic and magnetic properties of Sc_2CF_2 monolayer. *Int. J. Quantum Chem.* **2021**, *121*, e26666. [CrossRef]
112. Zhang, R.-Z.; Cui, X.-H.; Li, S.-S.; Li, X.-H.; Cui, H.-L. DFT computation of quantum capacitance of transition-metals and vacancy doped Sc_2CF_2 MXene for supercapacitor applications. *J. Mol. Liq.* **2022**, *345*, 118263. [CrossRef]

113. Cui, X.-H.; Li, X.-H.; Zhang, R.-Z.; Cui, H.-L.; Yan, H.-T. Computational study of intrinsic defects on the electronic properties and quantum capacitance of Sc_2CF_2 monolayer. *Surf. Interfaces* **2022**, *33*, 102193. [CrossRef]
114. Zha, X.H.; Huang, Q.; He, J.; He, H.; Zhai, J.; Francisco, J.S.; Du, S. The thermal and electrical properties of the promising semiconductor MXene Hf_2CO_2. *Sci. Rep.* **2016**, *6*, 27971. [CrossRef] [PubMed]
115. Wang, Y.; Ma, S.; Wang, L.; Jiao, Z. A novel highly selective and sensitive NH_3 gas sensor based on monolayer Hf_2CO_2. *Appl. Surf. Sci.* **2019**, *492*, 116–124. [CrossRef]
116. Liu, M.-Z.; Li, X.-H.; Cui, X.-H.; Yan, H.-T.; Zhang, R.-Z.; Cui, H.-L. The influence of different functional groups on quantum capacitance, electronic and optical properties of Hf_2C MXene. *Appl. Surf. Sci.* **2022**, *605*, 154830. [CrossRef]
117. Lei, J.-C.; Zhang, X.; Zhou, Z. Recent advances in MXene: Preparation, properties, and applications. *Front. Phys.* **2015**, *10*, 276–286. [CrossRef]
118. Liu, M.-Z.; Li, X.-H.; Yan, H.-T.; Zhang, R.-Z.; Cui, H.-L. Influence of N-doped concentration on the electronic properties and quantum capacitance of Hf_2CO_2 MXene. *Vacuum* **2023**, *210*, 111826. [CrossRef]
119. Cui, X.-H.; Li, X.-H.; Jin, X.-J.; Yan, H.-T.; Zhang, R.-Z.; Cui, H.-L. Biaxial strain tunable quantum capacitance and photocatalytic properties of Hf_2CO_2 monolayer. *Appl. Surf. Sci.* **2023**, *616*, 156579. [CrossRef]
120. Li, S.-S.; Li, X.-H.; Cui, X.-H.; Zhang, R.-Z.; Cui, H.-L. Effect of the biaxial strain on the electronic structure, quantum capacitance of NH_3 adsorption on pristine Hf_2CO_2 MXene using first-principles calculations. *Appl. Surf. Sci.* **2022**, *575*, 151659. [CrossRef]
121. Li, X.-H.; Cui, X.-H.; Xing, C.-H.; Cui, H.-L.; Zhang, R.-Z. Strain-tunable electronic and optical properties of Zr_2CO_2 MXene and $MoSe_2$ van der Waals heterojunction: A first principles calculation. *Appl. Surf. Sci.* **2021**, *548*, 149249. [CrossRef]
122. Mostafaei, A.; Faizabadi, E.; Semiromi, E.H. Theoretical studies and tuning the electronic and optical properties of Zr_2CO_2 monolayer using biaxial strain effect: Modified Becke–Johnson calculation. *Physica. E Low Dimens. Syst. Nanostruct.* **2019**, *114*, 113559. [CrossRef]
123. Xu, S.; Wang, S.J.; Sun, W.Q.; Li, X.H.; Cui, H.L. Density functional theory study of the electronic properties and quantum capacitance of pure and doped Zr_2CO_2 as electrode of supercapacitors. *Int. J. Quantum. Chem.* **2021**, *122*, e26844. [CrossRef]
124. Li, X.-H.; Jia, H.-Y.; Li, S.-S.; Cui, H.-L. Effect of atomic vacancy on the electronic and optical properties, quantum capacitance of Zr_2CO_2-based electrodes. *Vacuum* **2021**, *190*, 110284. [CrossRef]
125. Yin, S.H.; Cui, X.H.; Li, X.H.; Wang, S.J.; Zhang, R.Z.; Cui, H.L.; Yan, H.T. Theoretical study on the electronic properties and quantum capacitance of Zr_2CO_2 MXene with atomic swap. *Int. J. Quantum. Chem.* **2023**, *125*, e27135. [CrossRef]
126. Bai, L.; Yin, H.; Wu, L.; Zhang, X. First-principle study of the $Nb_{n+1}C_nT_2$ systems as electrode materials for supercapacitors. *Comput. Mater. Sci.* **2018**, *143*, 225–231. [CrossRef]
127. Xin, Y.; Yu, Y.-X. Possibility of bare and functionalized niobium carbide MXenes for electrode materials of supercapacitors and field emitters. *Mater. Des.* **2017**, *130*, 512–520. [CrossRef]
128. Bharti; Ahmed, G.; Kumar, Y.; Bocchetta, P.; Sharma, S. Determination of Quantum Capacitance of Niobium Nitrides Nb_2N and Nb_4N_3 for Supercapacitor Applications. *J. Compos. Sci.* **2021**, *5*, 85. [CrossRef]
129. Hussain, S.; Rabani, I.; Vikraman, D.; Feroze, A.; Ali, M.; Seo, Y.-S.; Song, W.; An, K.-S.; Kim, H.-S.; Chun, S.-H.; et al. MoS_2@X_2C (X = Mo or W) hybrids for enhanced supercapacitor and hydrogen evolution performances. *Chem. Eng. J.* **2021**, *421*, 127843. [CrossRef]
130. Hussain, S.; Faizan, M.; Vikraman, D.; Rabani, I.; Ali, B.; Kim, H.-S.; Jung, J.; Nam, K.-W. Eutectoid W_XC embedded WS_2 nanosheets as a hybrid composite anode for lithium-ion batteries. *Ceram. Int.* **2021**, *47*, 18646–18655. [CrossRef]
131. Poudel, M.B.; Logeshwaran, N.; Kim, A.R.; Karthikeyan, S.C.; Vijayapradeep, S.; Yoo, D.J. Integrated core-shell assembly of Ni_3S_2 nanowires and CoMoP nanosheets as highly efficient bifunctional electrocatalysts for overall water splitting. *J. Alloys Compd.* **2023**, *960*, 170678. [CrossRef]
132. Lu, C.; Zhang, Y.-S.; Hu, Y.-X.; Li, J.; Zhang, B.-M.; Liu, M.-C. Ultrafine Mo_2C nanoparticles supported on three-dimensional hierarchical porous carbon architecture toward electrochemical energy storage applications. *J. Energy Storage* **2021**, *33*, 101855. [CrossRef]
133. Dall'Agnese, Y.; Taberna, P.L.; Gogotsi, Y.; Simon, P. Two-Dimensional Vanadium Carbide (MXene) as Positive Electrode for Sodium-Ion Capacitors. *J. Phys. Chem. Lett.* **2015**, *6*, 2305–2309. [CrossRef]
134. Ai, W.; Zhang, C.; Xia, L.; Miao, H.; Yuan, J. Synthesis of High-Quality Two-Dimensional V_2C MXene for Supercapacitor Application. *Energies* **2022**, *15*, 3696. [CrossRef]
135. Bharti; Kumar, Y.; Gupta, M.; Sharma, S. Study of pristine and functionalized V_2C and Mo_2C MXenes as novel electrode material for supercapacitors. *J. Mol. Graph. Model.* **2023**, *118*, 108366. [CrossRef]
136. Karade, S.S.; Dwivedi, P.; Majumder, S.; Pandit, B.; Sankapal, B.R. First report on a FeS-based 2 V operating flexible solid-state symmetric supercapacitor device. *Sustain. Energy Fuels* **2017**, *1*, 1366–1375. [CrossRef]
137. Yu, F.; Chang, Z.; Yuan, X.; Wang, F.; Zhu, Y.; Fu, L.; Chen, Y.; Wang, H.; Wu, Y.; Li, W. Ultrathin $NiCo_2S_4$@graphene with a core–shell structure as a high performance positive electrode for hybrid supercapacitors. *J. Mater. Chem. A* **2018**, *6*, 5856–5861. [CrossRef]
138. Rui, X.; Tan, H.; Yan, Q. Nanostructured metal sulfides for energy storage. *Nanoscale* **2014**, *6*, 9889–9924. [CrossRef] [PubMed]
139. Septianto, R.D.; Liu, L.; Iskandar, F.; Matsushita, N.; Iwasa, Y.; Bisri, S.Z. On-demand tuning of charge accumulation and carrier mobility in quantum dot solids for electron transport and energy storage devices. *NPG Asia Mater.* **2020**, *12*, 2–14. [CrossRef]

140. Lin, Y.C.; Dumcenco, D.O.; Huang, Y.S.; Suenaga, K. Atomic mechanism of the semiconducting-to-metallic phase transition in single-layered MoS_2. *Nat. Nanotechnol.* **2014**, *9*, 391–396. [CrossRef]
141. Ali, B.A.; Metwalli, O.I.; Khalil, A.S.G.; Allam, N.K. Unveiling the Effect of the Structure of Carbon Material on the Charge Storage Mechanism in MoS_2-Based Supercapacitors. *ACS Omega* **2018**, *3*, 16301–16308. [CrossRef] [PubMed]
142. Yin, X.; Wang, Q.; Cao, L.; Tang, C.S.; Luo, X.; Zheng, Y.; Wong, L.M.; Wang, S.J.; Quek, S.Y.; Zhang, W.; et al. Tunable inverted gap in monolayer quasi-metallic MoS_2 induced by strong charge-lattice coupling. *Nat. Commun.* **2017**, *8*, 006402. [CrossRef] [PubMed]
143. Singh, N.; Schwingenschlogl, U. A Route to Permanent Valley Polarization in Monolayer MoS_2. *Adv. Mater.* **2017**, *29*, 1600970. [CrossRef] [PubMed]
144. Nie, Z.; Long, R.; Teguh, J.S.; Huang, C.-C.; Hewak, D.W.; Yeow, E.K.L.; Shen, Z.; Prezhdo, O.V.; Loh, Z.-H. Ultrafast Electron and Hole Relaxation Pathways in Few-Layer MoS_2. *J. Phys. Chem. C* **2015**, *119*, 20698–20708. [CrossRef]
145. Xu, Q.; Yang, G.M.; Zheng, W.T. DFT calculation for stability and quantum capacitance of MoS2 monolayer-based electrode materials. *Mater. Today Commun.* **2020**, *22*, 100772. [CrossRef]
146. Biby, A.H.; Ali, B.A.; Allam, N.K. Interplay of quantum capacitance with Van der Waals forces, intercalation, co-intercalation, and the number of MoS_2 layers. *Mater. Today Energy* **2021**, *20*, 100677. [CrossRef]
147. Irham, M.A.; Muttaqien, F.; Bisri, S.Z.; Iskandar, F. Enhancing quantum capacitance of iron sulfide supercapacitor through defect-engineering: A first-principles calculation. *Electrochim. Acta* **2023**, *449*, 142235. [CrossRef]